CFD-BASED MODELING OF MULTIPHASE FLOWS: FROM SPOUT BEDS TO HYDRAULIC FRACTURING

by

Md Omar Reza

A thesis submitted in partial fulfillment of the requirements for the degree of

Master of Science

in

Chemical Engineering

Department of Chemical and Materials Engineering
University of Alberta

Abstract

This work is devoted to the CFD analysis of multiphase flow using Euler-Euler model. In particular, Euler-Euler muliphase model is applied to study numerically the behaviour of gas-solid system and solid-liquid system. The main objective of this work is to validate Euler-Euler multiphase model available by commercial software FLUENT 14.0 against experimental results published by He et. al. [1, 2]. First part of this work relates to the transient dynamics of spouted bed which is a multiphase flow system with the presence of solid and gas phases. The comparison of simulation results showed acceptable agreement in the spout and good agreement in the fountain of a spout bed. We also study the influence of basic parameters on the model performances. Second part of this work is devoted to the CFD analysis of hydraulic fracturing which is also a multiphase flow system where solid and liquid phase is present. The main goal is to study numerically hydraulic fracturing using Euler-Euler multiphase flow model from FLUENT 14.0[3] and to validate it against Euler-Lagrange model[4].

Acknowledgements

At first I would like to thank my lord for making me capable of working on something that I truly enjoyed. I would like to express my deepest and sincere gratitude to my thesis supervisor, *Dr. Petr Nikrityuk* for his constant encouragement and advice throughout my study. Without his warm support and immense knowledge, this thesis could not be completed. I am also grateful to *Dr. Subir Bhattacharjee*, my previous supervisor with whom I initially started working in University of Alberta and gained some valuable research experiences.

I would also like to give a special thanks to my research group mate, Pankaj Kumar Sahu for being so helpful in all my difficulties and providing with thoughtful suggestions. I also want to thank Nitish Ranjan Sarkar and Md Ashker Ibn Rashid for their help and support throughout my course work and research activity.

A special gratitude goes to my family, and especially my parents for their continuous support throughout my life. This thesis would be impossible without them. My heartfelt thanks to my wife Saadia Pinky, who has been the key to my success. I am also taking this opportunity to thank all my friends. Without them, life will become very dull.

Table of Contents

List of Figures

List of Tables

List of Symbols

α_q	volume fraction of q phase
V_q	volume of phase q
$\hat{\rho}_q$	effective density of phase q
ρ_q	physical density of phase q
$\vec{v}_q$	velocity of phase q
$\overline{\overline{\tau}}_q$	q^{th} phase stress-strain tensor
g	gravitational acceleration
p	pressure shared by all phases
$\vec{R}_{pq}$	interaction force between phases
μ_q	shear viscosity of phase q
λ_q	bulk viscosity of phase q
K_{pq}	interphase momentum exchange coefficient
v_g	velocity of gas phase
v_s	velocity of solid phase
K_{gs}	interphase momentum exchange coefficient between gas and solid phase
α_s	volume fraction of solid phase
α_g	volume fraction of gas phase
C_D	drag function
Re_s	Reynolds number for solid particles

d_s, d_p	diameter of solid particle
$v_{r,s}$	terminal velocity correlation for the solid phase
A, B	constant value for Syamlal-O'Brein drag model
p_s	solid pressure
γ_{θ_s}	collisional energy dissipation
ϕ_{gs}	kinetic energy transfer
e_{ss}	coefficient of restitution
θ_s	granular temperature
$g_{0,ss}$	radial distribution function
$\alpha_{s,max}$	maximum packing limit
μ_s	solid shear viscosity
$\mu_{s,col}$	solid collisional viscosity
$\mu_{s,kin}$	solid kinetic viscosity
$\mu_{s,fr}$	frictional viscosity
μ_g	viscosity of gas phase
$\overline{U}_s$	volume averaged velocity for solid phase
$\overline{U}_g$	volume averaged velocity for gas phase
$U_{in,g}$	inlet velocity of gas phase
$U_{in,s}$	inlet velocity of solid phase
U_{ms}	minimum spouting velocity
d_{in}	inlet diameter of spouted bed reactor
$d_{reactor}$	diameter of spouted bed reactor
St	Stokes number

τ_d	particle response time
t_s	system response time
L_s	characteristic length of system
V_s	velocity of system under investigation
V_{sb}	volume of the whole spout bed reactor
v_θ	swirling ratio
t	time
H	height from inlet of spouted bed
D	fracture height
CV	control volume
μ_R	viscosity ratio of system water with the viscosity of regular water
L_{mix}	length of mixing zone
ϕ_s	volume fraction of solid phase

Subscripts

l	liquid phase
g	gas phase
p	particle
s	solid phase

Chapter 1

Introduction - Multiphase Flow Modeling Concepts

Recent development of both computer hardware and computational software have lead this world to solve complex problems; physically or geometrically in a much cheaper way with lesser effort. The very first numerical model was developed to model the process of nuclear detonation during the Manhattan project in World War II [8]. Since then the numerical modeling is widely used approach to solve complex mathematical problems in variety of natural systems in physics (computational physics), astrophysics, chemistry and biology, human systems in economics, psychology, social science, and engineering. Sometimes experimental investigations are too expensive to begin with and numerical modeling gives a cheaper solution. Because of numerical modeling, it is now possible to investigate the processes that are impossible to measure. For example, it is quite impossible to measure the propagation of mixing zone inside a hydraulic fracturing, but numerical modeling made it possible to access, measure and investigate such kind of processes. Moreover, numer-

ical simulation can be used to calculate the optimum parameters for existing industrial machinery and equipment and improve the design to provide next generation devices. However, wrong model selection and imperfect settings of the simulation process may lead the simulation result deviating from reality.

CFD modeling of multiphase flow has become widely accepted to the scientists and researcher because of its broad range of application and contribution to the 'reservoir of knowledge'. A lot of research on CFD simulation of multiphase flows have been conducted to predict the behaviour of fluidized bed [9, 10, 11], slurry transportation [12, 13], spray drying [14, 15], pulverized coal fired furnaces [16], pneumatic transportation [17], plasma spray coating [18], solid propellant rockets and spray forming [19] etc. Inside multiphase equipment the particles collide, shear and interact; exchange of momentum occurs between particles and fluids with interaction of device boundaries; interchange of heat and mass occurs; sometimes different kind of chemical reaction takes place at different scale. There are several approaches to describe multiphase flows; some of them need intensive processing while some of them need laborious modeling effort. Higher physical resolution decreases the modeling labour but rises the computational price.

Multiphase flow modeling can be divided into two main categories: i) disperse multiphase flows ii) continuous multiphase flows. Euler-Lagrange method is widely used numerical approach to describe multiphase flow that is suitable only for disperse flows. In this method, the continuous phase is investigated in an Eulerian manner by solving the time-averaged Navier-Stokes equations, whereas the disperse phase is investigated in a Lagrangian manner. In Lagrangian approach individual particles are tracked through the computed flow field by solving Navier-Stokes equations and Newton's equations of motion

for each particle [20, 21, 22]; the velocity and position of an individual particle is a function of time only. From the literature [9, 10], these class of models are generally called discrete particle models (DPMs) or discrete element models (DEMs). This model uses subgrid zero-equatoin (0-D) models for particles and fluid heat and mass transfer modeling [23, 24] which is one of the major limitations of this model. Following the classification from literature, DPM-based Euler-Lagrange models can be sub-divided according to the coupling method of the Euler and the Lagrange phases into unresolved discrete particle model (UDPM) or resolved discrete particle model (RDPM). In UDPM model, the Eulerian grid has to be at least an order of magnitude larger than the particle size. The particle-particle interaction in UDPM is modeled in two ways: hard sphere and soft sphere model. The soft sphere model has become more popular because of it's capability to handle a large number of particles ($> 10^6$) [25]. On the other hand, RDPM model uses the Eulerian grid, but at least an order of magnitude smaller than the particle size [11]. In literature, RDPM is often refereed as the direct numerical simulation (DNS) model. The UDPM based Euler-Lagrange models are widely used tools for macroscale simulations of transport processes; on the other hand, DNS Euler˙Lagrange models are popular for micro and mesoscale processes. However, both of the Euler-Lagrange models are extremely time consuming and an expensive computational choice. But Euler-Lagrange method is cheaper in a sense of modeling though expensive in the sense of computation.The size of the system as well as the physics that can be described by this method is limited. So, it is not realistic to model a system with billions of particles using Euler-Lagrange method. On the other hand, Euler-Euler method is popular for industrial applications because of its cheaper computational time, but it requires a significant amount of modeling

effort. In this method, the discrete particles equations of motions are averaged; the resulting continuum-solids phase behave like fluid phase; which results an inter penetrating continuum model. For this reason, a large number particles do not effect the computational price extensively. However, an expensive price must be paid to the modeling effort. Nowadays"multiphase flow modleing of disperse flow using Euler-Euler method" is a challenging topic of ongoing research and we conducted our research on "spouted bed" and "hydrodynamic fracturing" using Euler-Euler approach to solve some of the 'unknown' behaviors which still exist in the present systems. In this view validation of multiphase models and software against reliable data plays an important role for the judgment of model acceptability to real processes. From this point, we validate our Euler-Euler model for slid-gas system with most popular and robust work of He at. el. [1, 2]. Authors used fiber optic image probe technique to measure the profile of vertical solid velocities, fountain height for half and full-column spouted bed. They also determined the voidage profile in different region of spouted bed and concluded some voidage characteristics. Our results showed a very good agreement with experimental data. The detailed description of the results can be found in chapter 2.

Next, we validate Euler-Euler model with liquid-slid system against Euler-Lagrange model for particle sedimentation. Relatively good agreement was achieved and based on that we apply Euler-Euler model for CFD analysis of hydraulic fracturing. Main results and detailed explanation are discussed in chapter 3.

Chapter 2

Euler-Euler Based Modeling of a Spouted Bed

2.1 State of Art

Impressive development of computational fluid dynamics (CFD) software (commercial and non-commercial) and computational hardware (multiprocessor PC) made it possible to carry out sophisticated 'numerical experiments'. Such numerical experiments allow engineers to understand many complex processes which are inaccessible for measurements. In this view, the bottleneck of such virtual experiments is a validation of a software. Applied to numerical modeling any software validation against experimental data plays the role of a bridge between real processes and processes modeled using different physical, mathematical and numerical approaches. Utilization of CFD in chemical engineering becomes more and more popular due to reduction of costs and time for the design of new chemical reactors [26]. Applied to CFD-based modeling of fluidized and spouted bed, commercial CFD software has only recently been

explored as a powerful tool in designing, scaling and optimizing beds and their working parameters. e.g. see the representative works [5, 27, 28, 29, 30, 31, 32]. Spouted bed technique, which was originally discovered in Canada by Mathus and Gishler [33] became a widely used operation for drying, pyrolysis and gasification. It was invented to deal with relatively large size or coarse particles. In spouted bed coarse solid particles are placed under appropriate conditions usually in a holding carrier to cause the solid/fluid mixture to behave like a fluid. Usually pressurized fluid is introduced through the solid particulate medium. This results in the medium then having many properties and characteristics of normal fluids; such as the ability to free-flow under gravity; or to be pumped using fluid type technologies. So, the interest to understand spouted beds become more and more popular amongst the scientists and researchers. As a result, increasing interest to understand and to optimize basic operating conditions has lead to large number of works devoted to CFD-based modeling of spout-bed systems[34, 35, 5, 27].

2.1.1 Experimental Work - Benchmark Tests

Amongst all of the experimental work done by researchers, the work done by He et. al. [1] has become the most popular and the most cited research. Authors used fiber optic probe technique with fully cylindrical Plexiglas column of inside diameter $152mm$ and height $1.4m$. Conical base angle was 60^o and inlet orifice diameter was $19mm$. Few experiments were carried out with same diameter, base angle and orifice diameter but half-column. In the first work, authors experimentally determined the vertical particle velocity profiles in the spout and the fountain of a full-column and half-column spouted bed. To de-

termine the spout-annulus interface and to measure vertical particle velocities in the annulus of the full- columns authors used a fiber optic image probe in the annulus of the full-column. They found that, radial profiles of vertical particle velocities were of near Gaussian distribution. Under identical operating conditions, particle velocities along the spout axis in the half-column were 30% lower than in the full-column. The fountain core expanded suddenly near the bed surface and then gradually contracted with height.

In another work [2], authors measured the voidage profiles in spouted beds. They used the same experimental technique and successfully measured voidage profiles in the fountain, spout and annulus of spouted beds. They found that the voidage in the annulus is higher than the loose-packed voidage and that it increase with increasing gas flow rate, except for a restricted region near the spout-annulus interface. They also found that the voidage is lower than the loose-packed bed voidage in the denser region of the annulus near the spout interface. Local voidage decreases with height and radial distance from the spout axis in spout region.

Qian et. al. [36] investigated solid volume fraction using novel fiber high speed photography method. They used high speed photography method to accomplish this work. The experimental system consists of a small fiber-optic endoscope, a halogen light source, a high speed video recorder and a computer. The results show that the radial profile of solid volume fraction decreases from the centre to the bed wall in the case of constant superficial gas velocity. All experimental results agrees with the results of He et. al. [1].

Xu et. al. [37] investigated flow pattern and transition in gasliquidsolid three phase spouted bed experimentally. Experimental method was developed depending on the pressure drop changes and taking photographs. Set-up

was consists of a conical-cylindrical Plexiglas column, a gas supply, a water adding system, an imaging system and a multi-channel differential pressure signal sampling system. Authors investigated spouted bed with spherical particles experimentally. They predicted the characteristics of flow patterns and pressure drop in the spouted bed. They also predicted the influences of the particle diameter and bed height on the flow pattern transition. Authors identified and described five distinct flow patterns: fix bed, grain spouting, cluster spouting with slugging, solid fixed with gas-liquid bubbling and slurry agitated bed. There are several works devoted to combined experimental and numerical study. In next section, we discuss some of those.

Link et. al. [38], investigated the flow regimes in a spouted bed by doing a combined experimental and simulation study. For the experiment, they used spectral analysis of pressure drop fluctuations and fast video recordings technique and for simulation, they used Euler-Lagrange discrete particle model (DPM). High frequency pressure probe was used to measure bed pressure drop at 100 Hz. Images were recorded with 262 Hz CCD camera equipped with 12.5mm lens. Authors wanted to design a model which has the ability to reproduce several important regimes in spout-fluid bed. The model was capable of predicting appropriate regimes in most of the cases. Their model could predict the frequency at which the largest power was found. But the limitation of the model was, it could not predict any large slugs in the slugging bed regime.

In another work, Link et. al. [39] conducted experimental and numerical study to gain the insight into the hydrodynamics of spouted bed. For the experiment, they recorded 500 digital images over a period of 2 seconds. PIV was used to obtain particle velocity profiles and bubble detection was used to

obtain voidage profiles on the same grid. For the simulation, they used discrete particle model with coefficient of restitution of 0.97 ± 0.01, coefficient of friction of 0.10 ± 0.01, size of computational cells of 10 x 10 x 15 mm, time step of $1\text{x}10^{-04}$ second and total simulation time of 5 seconds. They found that the simulated particle fluxes are generally higher than the experimentally measured one. It was also found that the voidage profiles are less accurate when particles move at high velocity. Their experiments showed the influence of the spout velocity on the bed penetration and the influence of the background fluidization velocity on the overall particle behavior.

Bettega et. al. [40] investigated the influence of the flat wall in the solid behavior inside the semi-cylindrical vessel. They have done both experimental study and numerical simulation to carry on their investigation. Their experimental set-up includes a blower, a heat exchanger, a system of data acquisition and a semi-cylindrical conical spouted bed. The data acquisition unit was composed by thermocouples, pressure transducer, image capture device, data acquisition boards and microcomputer. For the numerical study, they used Euler-Euler model from commercial code of FLUENT 6.3.26. SIMPLE algorithm was used to solve pressure-velocity coupling. First order discretization for momentum and volume fraction variables was used. The under-relaxation factor was taken between 0 and 0.5. The system was considered steady state after 8s of real life simulation. Time step was taken between 1x 10^{-04} and 5x 10^{-04} seconds. They found a good agreement between numerical and experimental study. According to their numerical study, the solid phase dynamic behavior tends to disturb the flow inside the vessel, even the friction between solid phase and flat wall was neglected.

In another work, Bettega et. al. [41] invented the scale-up study of spouted

beds using computational fluid dynamics. They used the same numerical setting but time step taken between $1x10^{-04}$ and $1x10^{-03}$ seconds. Authors investigated scaling relationships proposed by He et al. [42] for spouted bed systems based on similitude method using CFD simulation. They found that if all of the scale-up relations are fulfilled, numerical simulation shows good results. They also concluded that for analyzing similitude method in spouted bed, CFD simulation is pretty useful.

Gryczka et al. [43] investigated CFD modeling of a prismatic spouted bed with two adjustable gas inlets. They used the commercial code of FLUENT 6.2 with Euler-Euler approach. Simulations were compared with the experimental results found by PIV measurements. They found an improved agreement with the experiment when they used Clift et al. [44] drag model. Zhonghua et. al.

Shirvanian et. al.[45] developed a 3D Eulerian simulation of rectangular spouted bed to describe iso thermal, two-phase flow of the continuous and dispersed phases. For the experimental part they used a micro pitot tube constructed by Aeroprobe Corporation to measure pressure and three velocity components. Micro pitot tube consists of five probes of 0.508 mm, pressure transducer, data acquisition system CIO-DAS08. Two 40.6cm x 40.6 cm x 35.6 cm Plexiglas were used as front and back of spouted bed. For simulation, they used Eulerian-Eulerian model with k-epsilon turbulence model. First 3s of real time simulation was done by assuming laminar flow. Then turbulence model was used for both solid and liquid phase. Time step was taken 0.001s and total real time simulation was for 20s.

2.1.2 CFD based modeling

Zhonghua et. al. [46] investigated CFD modeling of the gas-particle flow behavior in spouted beds. They used commercial code of FLUENT version 6.2 taking Eulerian-Eulerian approach into account. They also included Gidapow's drag model and Lun's granular kinetic theory. To include effects of turbulent fluctuations of velocities and scalar quantities in the gas phase, they used k-epsilon turbulence model. SIMPLEC algorithm was used to couple pressure-velocity term. Under relaxation factors were take between 0.2-0.4. Residuals for temperature, velocity were less than $1x10^3$. Authors predicted gas-solid flow behavior in two types of spouted beds using numerical simulation and compared with recent experimental results. The flow instabilities of the spout-fluid bed was presented and possible formation mechanism was discussed.

Huilin et. al. [35] investigated hydrodynamics of gas-solid flow in spouted beds using two-fluid model. Computed radial profiles of particle velocities and volume fraction were in good agreement with the measurements obtained by He et al.[1, 2]. However, authors did not compare axial profiles of particle velocity against experimental data.

Du et. al. [5, 27] carried out numerous CFD-based simulations of spouted bed in respect to the influence of different drag models, maximum packing limit, coefficient of restitution on the characteristics of the spouted bed investigated experimentally by He et. al. [1, 2]. Authors used RANS-based Euler-Euler model. The comparison against experimental data by He et al. showed qualitative agreement. They found that the frictional stress is important in the annulus and has a slight effect on the hydrodynamics of the flow in

the spout region. The maximum packing limit affects the radial distribution function and thereby impacts the estimation of the properties of the pseudo-fluid phase of the particles. They also found that the strong dependence of the granular temperature on the coefficient of restitution accounts for the influence of the latter on the CFD modeling of the spouted bed.

In spite of numerous numerical investigations of the spouted bed systems there is still a lack of understanding the transient dynamics of spouted beds, e.g. what is the start-up time, what are the fountain oscillation periods and their relations with model conditions (e.g. restitution coefficient and packing limit)? All of the CFD simulations done so far [5, 27, 46, 43] considered RANS based Euler-Euler model to simulate spouted bed. But we found that the global Reynolds number for particles does not indicate turbulence at all. Also there is still uncertainty regarding which combination of "drag model" and "restitution coefficient" is most suitable for spout bed. To answer these questions we use commercial CFD software ANSYS-Fluent 14.0.[3] to carry out unsteady numerical simulations of an axisymmetric spouted bed which geometry and inflow conditions corresponds to the bed investigated experimentally by He et al [1, 2]. We also studied the effect of swirling velocity in the flow dynamics of spouted bed successfully.

2.2 Problem and Model Description

In the Eulerian-Eulerian approach, the fluid (gas) and dispersed phase (particles) are treated mathematically as inter-penetrating continua using conservation equations averaged over *representative elementary volume* (REV) for each phase. Volume fractions of the overlapping phases are assumed to be

continuous functions of space and time. Volume fractions represent the space occupied by each phase, and the laws of conservation of mass and momentum are satisfied by each phase individually. Their sum equals to unity. The model equations were adopted from ANSYS FLUENT user guide [7].

2.3 List of Assumptions

Before we proceed with the model formulation we introduce basic assuptions we use:

- **Flow is unsteady laminar:** this assumption is based on the different Reynolds numbers calculated using variour characteristic scales. In particular, we calculate Reynolds number for particles and gas at different location of spouted bed as follows:
  - Reynolds for particles at inlet region:

$$Re = \frac{\rho_g |U_{g,in} - U_{s,in}| d_p}{\mu_g} = \frac{1.225 \cdot |44 - 7| \cdot 1.41 \cdot 10^{-3}}{1.7894 \cdot 10^{-5}} = 3.5715 \cdot 10^3 \tag{2.1}$$

  - Reynolds for particles inside column:

$$Re = \frac{\rho_g \left|\overline{U}_s - \overline{U}_g\right| d_p}{\mu_g} = \frac{1.225 \cdot |1.15 - 0.55| \cdot 1.41 \cdot 10^{-3}}{1.7894 \cdot 10^{-5}} = 57.92 \tag{2.2}$$

  - Reynolds for gas at inlet region:

$$Re = \frac{\rho_g U_{in,g} d_{in}}{\mu_g} = \frac{1.225 \cdot 44 \cdot 19 \cdot 10^{-3}}{1.7894 \cdot 10^{-5}} = 58.39946 \cdot 10^3 \tag{2.3}$$

Name	*Equation*
Volume of phase	$V_q = \int_v \alpha_q dv$
Volume fraction balance	$\sum_{q=1}^{n} \alpha_q = 1$
Effective density	$\hat{\rho_q} = \alpha_q \rho_q$
Continuity equation	$\frac{\partial}{\partial t}\left(\alpha_q \rho_q\right) + \nabla \cdot \left(\alpha_q \rho_q \vec{v_q}\right) = 0$
Momentum balance	$\frac{\partial}{\partial t}\left(\alpha_q \rho_q \vec{v_q}\right) + \nabla \cdot \left(\alpha_q \rho_q \vec{v_q} \vec{v_q}\right) = -\alpha_q \nabla p + \nabla \cdot \overline{\overline{\tau_q}} + \alpha_q \rho_q \vec{g} + \sum_{p=1}^{n} \vec{R}_{pq}$
Solid phase stress tensor	$\overline{\overline{\tau_q}} = \alpha_q \mu_q \left(\nabla \vec{v_q}^T\right) + \alpha_q \left(\lambda_q - \frac{2}{3}\mu_q\right) \nabla \cdot \vec{v_q} \overline{\overline{I}}$
Interphase force	$\sum_{p=1}^{n} \vec{R}_{pq} = \sum_{p=1}^{n} K_{pq}\left(\vec{v_p} - \vec{v_q}\right) = \sum_{p=1}^{n} K_{gs}\left(\vec{v_s} - \vec{v_g}\right)$
Syamlal-O'Brien drag model	$K_{gs} = \frac{3\alpha_s \alpha_g \rho_g}{4 v_{r,s}^2 d_s} C_D \left(\frac{Re_s}{v_{r,s}}\right) \left\lvert \vec{v_s} - \vec{v_g} \right\rvert$, $C_D = \left(0.63 + \frac{4.8}{\sqrt{Re_s / v_{r,s}}}\right)^2$ $v_{r,s} = 0.5\left(A - 0.06 Re_s + \sqrt{0.06 {Re_s}^2 + 0.12 Re_s (2B - A) + A^2}\right)$ For $\alpha_g \leq 0.85$, $A = \alpha_g^{4.14}$, $B = 0.8\alpha_g^{1.28}$ For $\alpha_g > 0.85$, $A = \alpha_g^{4.14}$, $B = \alpha_g^2.65$
Wen-Yu drag model	$K_{gs} = \frac{3}{4} C_D \frac{\alpha_s \alpha_g \rho_g \left\lvert \vec{v_s} - \vec{v_g} \right\rvert}{d_s}$, $C_D = \frac{24}{\alpha_s Re_s}\left[1 + 0.15\left(\alpha_g Re_s\right)^{0.687}\right]$
Gidaspow drag model	When $(\alpha_g > 0.8)$, $K_{gs} = \frac{3}{4} C_D \frac{\alpha_s \alpha_g \rho_g \left\lvert \vec{v_s} - \vec{v_g} \right\rvert}{d_s} \alpha_g^{-2.65}$, $C_D = \frac{24}{\alpha_g Re_s}\left[1 + 0.15\left(\alpha_g Re_s\right)^{0.687}\right]$ When $(\alpha_g \leq 0.8)$, $K_{gs} = 150 \frac{\alpha_s (1 - \alpha_g) \mu_g}{\alpha_g d_s^2} + 1.75 \frac{\alpha_s \rho_g \left\lvert \vec{v_s} - \vec{v_g} \right\rvert}{d_s}$
Transport equation (algebric)	$\left(-p_s \overline{\overline{I}} + \overline{\overline{\tau_s}}\right) : \nabla \vec{v_s} + \gamma_{\theta_s} + \phi_{gs} = 0$
Solid pressure	$p_s = \alpha_s \rho_s \theta_s + 2\rho_s\left(1 + e_{ss}\right)\alpha_s^2 g_{0,ss} \theta_s$
Radial distribution function	$g_{0,ss} = \left[1 - \left(\frac{\alpha_s}{\alpha_{s,max}}\right)^{\frac{1}{3}}\right]^{-1}$
Collisional energy dissipation	$\gamma_{\theta_s} = \frac{12\left(1 - e_{ss}^2\right) g_{0,ss}}{d_s \pi^{0.5}} \rho_s \alpha_s^2 \theta_s^{1.5}$
Kinetic energy transfer	$\phi_{gs} = -3 \cdot K_{g,s} \theta_s$
Solid shear viscosity	$\mu_s = \mu_{s,col} + \mu_{s,kin} + \mu_{s,fr}$
Collisional viscosity	$\mu_{s,col} = \frac{4}{5}\alpha_s \rho_s d_s g_{0,ss}\left(1 + e_{ss}\right)\left(\frac{\theta_s}{\pi}\right)^{1/2}$
Kinetic viscosity	$\mu_{s,kin} = \frac{10 \rho_s d_s \sqrt{\theta_s \pi}}{96 \alpha_s (1 + e_{ss}) g_{0,ss}}\left[1 + \frac{5}{4} g_{0,ss} \alpha_s \left(1 + e_{ss}\right)\right]^2$
Frictional viscosity	$\mu_{s,fr} = \frac{p_s sin\phi}{2\sqrt{I_{2D}}}$
Bulk viscosity	$\lambda_s = \frac{4}{3}\alpha_s \rho_s d_s g_{0,ss}\left(1 + e_{ss}\right)\left(\frac{\theta_s}{\pi}\right)^{1/2}$

Table 2.1: Model equations adopted from ANSYS FLUENT [7]

– Reynolds for gas inside column:

$$Re = \frac{\rho_g \overline{U}_g d_{reactor}}{\mu_g} = \frac{1.225 \cdot 44 \cdot 152 \cdot 10^{-3}}{1.7894 \cdot 10^{-5}} = 5.7231 \cdot 10^3 \quad (2.4)$$

We see here that the Reynolds number is high at the inlet region. So, the flow might be turbulent at inlet region. But the Reynolds inside the reactor for particles is only 57.92. For this reason, we utilize Euler-Euler unsteady laminar model. Initially we tried using RANS based turbulent model, but the model failed to predict spouted bed behaviour properly. Because we have presence of bubbles inside bed. Besides, for calculation of Reynolds number we used viscosity of air, which is not quite appropriate. We still do not know the transitional Reynolds number in available literature. So, taking unsteady laminar seems the best way to model multiphase flow for spouted bed.

- **Flow is axi-symmetric:** We have axi-symmetric geometry and in available literature, we found all of the simulations were done assuming axi-symmetric flow [27, 5]. For this reason, we are assuming flow is axi-symmetric to save computational price.

- **Lift and Virtual Mass Force Neglected:** For the simulation of spouted bed in majority of work, lift force and virtual mass force are neglected [47] page 59.

- **Models:** The list of models and schemes used for spout bed modeling are presented in Tables 2.1 and 2.2.

Name	*Model/ Scheme Name*
Multiphase Flow	Euler-Euler [7], pages (537-588)
Volume Fraction Parameters	Implicit Scheme [7], page (501)
Viscous Model	Unsteady Laminar
Drag Model	Syamlal-O'Brien [48], [7] pages (547-548)
Granular Temperature	Phase property [7] page (559)
Granular Viscosity	Syamlal-O'Brien [49], [7] page (557)
Granular Bulk Viscosity	Lun-et-al [50], [7] page (557)
Frictional Viscosity	Johnson-et-al [51], [7] page (557)
Frictional Pressure (pascal)	Johnson-et-al [51], [7] page (557)
Solid Pressure	Syamlal-O'Brien [49], [7] page (557) page (552)
Radial Distribution	Syamlal-O'Brien [52], [7] page (553)
Pressure-Velocity Coupling	Coupled Scheme [7] page (643)
Spatial Discretization-Gradient	Least Squares Cell Based [7] page (559)
Spatial Discretization-Momentum	QUICK [7] page (652)
Spatial Discretization-Volume Fraction	Modified HRIC [53], [7] page (653)
Transient Formulation	First Order Implicit [7] page (501)

Table 2.2: List of different models/ schemes used to model transient simulation of spout-bed

2.4 Numerical Parameters

To solve numerically momentum and mass conservation equations describing the behaviour of the spouted bed use so called pressure-based '*coupled algorithm*'[7], which solves the momentum and pressure-based continuity equations together. The full implicit coupling is achieved through an implicit discretization of pressure gradient terms in the momentum equations, and an implicit discretization of the face mass flux. For the discretization of convective terms in momentum conservation equations we utilize so called QUICK scheme[54]. For the discretization of convective terms in the equation for the calculation of the volume fraction of gas/solid we activate so called *modified HRIC* scheme, which is a modified version of the High Resolution Interface Capturing (HRIC) scheme[53]. The modified HRIC scheme is a composite

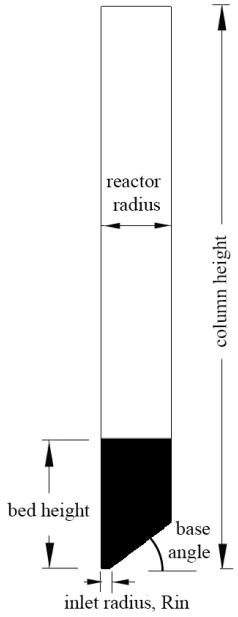

Name	*Measurement*
Reactor Radius	76 mm
Inlet Radius	9.5 mm
Column Height	1.41 m
Bed Height	0.325 m
Base Angle	60^o

Figure 2.1: Schematic diagram of spout bed indicating different geometric parameters with measurement

NVD scheme that consists of a non-linear blend of upwind and downwind differencing.

Computational domain corresponds to a cylindrical column of inside *diameter 152 mm* and *heigh 1.4m* corresponding to experimental conditions [1, 2]. The column has a conical base with a 60^0 included angle and an inlet orifice of *diameter 19 mm*.

The numerical grid using in this work comprises of $14 \cdot 10^3$ control volumes. Zoomed view of the spout region is shown in Fig. 2.2.

Inlet section comprises of 5 control volumes (CV) in the radial direction corresponding to the radial size of one CV of about $\Delta r = 1.9$ mm. The mean diameter of glass beads used in experiments[1, 2] is $d_p = 1.41$ mm. Thus, we have the ratio between Δr and d_p is $\frac{\Delta r}{d_p} > 1$.

The time step was set to 10^{-3} sec. Volume fraction equation for the gas phase was discretized in time using first-order implicit scheme. The number

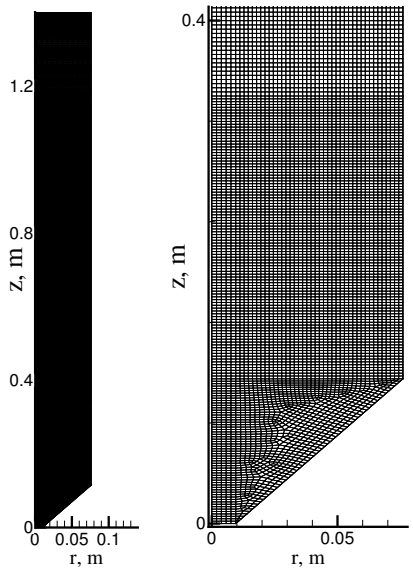

Figure 2.2: Computational axi-symmetric domain and grid, right figure is zoomed view of the grid.

of iteration per one time step was fixed to 40, which guarantees the maximum normalized residual of about 10^{-5} for each time step.

All simulations start from a static bed with a height of 0.325 m following experimental data by He et al [1, 2]. At the inlet orifice, the gas is injected with the fixed velocity of $u_z = 44$ m/s. Thus, the ratio $\frac{U}{U_{ms}} \approx 1.3$, where U is flow rate averaged axial velocity of the gas and $U_{ms} = 0.54$ m/s is the minimum spouting velocity according to experimental setup data[1]. At the outlet, outflow boundary condition was used for all dependent variables. On the wall, no slip boundary condition was used for both phases.

The corresponding input parameters used in simulations are listed below:

Stokes Number:

Relation between the particle response time and the system response time is

particle diameter, d_p (mm)	1.41
particle density, ρ_s (kg/m^3)	2503
Gas density, ρ_g (kg/m^3)	1.225
Gas viscosity, μ_g (Pa/s)	$1.7894 \cdot 10^{-5}$

Table 2.3: Input parameters used to model spouted bed.

defined as Stokes number [7] page 497:

$$St = \frac{\tau_p}{t_s} \tag{2.5}$$

Where,

Particle response time, $\tau_p = \frac{\rho_p d_p^2}{18\mu_g} = \frac{2503 \cdot \left(1.41 \cdot 10^{-3}\right)^2}{18 \cdot 1.74 \cdot 10^{-5}} = 15.89$ sec

System response time, $t_s = \frac{L_s}{V_s} = \frac{D_{reactor}}{|U_s - U_g|} = \frac{152 \cdot 10^{-3}}{1.15 - .55} = 0.253$ sec

Here,

L_s = Characteristic Length of the system

V_s = Velocity of system under investigation

So, Stokes Number, $St = \frac{15.89}{0.253} = 62.81$

2.5 Results

We discuss our simulation result step-by-step describing how we achieved our final goal. First, we validate our model and software with He et. al. [1, 2] experimental data. There we compare our result for axial and radial profile of the time-averaged velocity of particles, voidage profiles at different heights and spout profiles with experimental data. Then we show a comparative study between different drag models e.g. Syamlal and O'Brein drag model [49], Gidaspow drag model [55], Wen and Yu drag model [56] etc. We analyze different model parameters such as coefficient of restitution e_{ss}, maximum packing limit

$\alpha_{s,max}$ and initial packing etc. We study the effect of drag model and restitution coefficient on the transient dynamics of the spouted bed. Finally, we present the effect of swirling motion of inlet gas and there we discover some of the interesting behaviors of spouted bed that may benefit us in future.

Before we proceed with description of transient dynamics of a spout bed, we present the model and software validation. In particular, Fig. 2.3 shows the axial particle velocity profiles on the axis of the spout. It can be seen that particles are accelerated close to inlet orifice ($0 < z < 0.07$ m) and then particles decelerate due to the gravity force. The critical issue here is correct prediction of the fountain height, which corresponds to z coordinate when particle velocity approaches zero. We compare our results with experimental

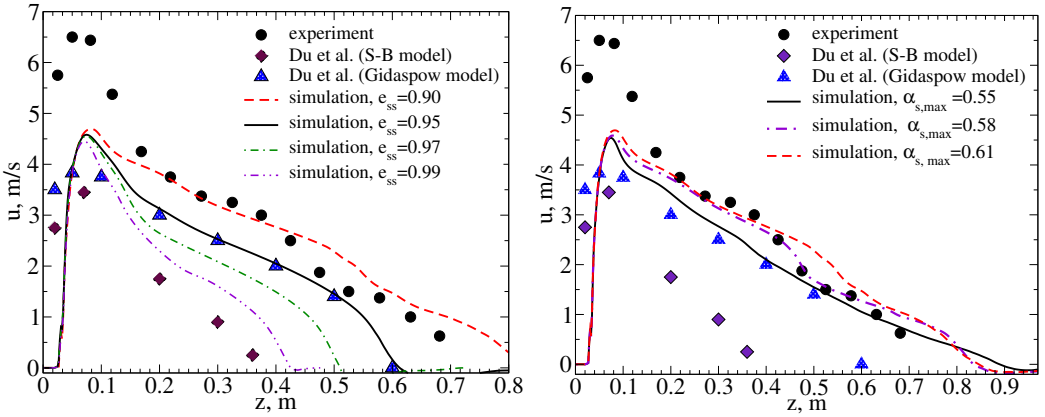

Figure 2.3: Axial profiles of the time-averaged velocity of the solid phase. Here 'experiment' data correspond to the work He et al. [2] and 'Due tal al' corresponds to the simulation work of Du et. al. [5], where 'S-B' means *Syamlal-O'Brien* drag model. Figure (a) shows simulation results for different e_{ss} with $\alpha_{s,max} = 0.61$ and (b) shows simulation results for different $\alpha_{s,max}$ with $e_{ss} = 0.90$

data from He et. al. [2] and simulation data given by Du et. al. [5] with two different drag models (Syamlal-O'Brien and Gidaspow model). It shows that our simulation result with $e_{ss} = 0.90$ is the best match with the experimental

data. The possible explanation of discrepancies could be the use of RANS model in [5] et. al. work. The Reynolds number for particles inside the reactor is only 67.09 and the Reynolds number for gas inside reactor is only 7284.00 which is not high turbulent at all. Though our result is slightly deviating near to the inlet region up to height of 0.12 m, but then it almost duplicates the experimental results for the rest of the height. Axial velocity of solid particles rapidly increases up to height of 0.1 m along the spout axis, then it steadily decreases. We also notice the effect of restitution coefficient on axial profile in figure 2.3 (a). The simulation result is highly influenced by the value of restitution coefficient. Because in Euler-Euler model, many of the solid-phase properties (i.e. solid bulk viscosity, solid pressure, solid shear viscosity etc.) are the function of restitution coefficient. So, the challenge is to determine the correct value of restitution coefficient which gives the closest result with experimental data. Here we see that the maximum spout height and the maximum value of axial velocity reduces when the value of e_{ss} increases. The explanation of this scenario is for higher value of e_{ss}, we get elastic collision between particles. For $e_{ss} = 1.0$, we get perfectly elastic collision and for that reason particles moves to the largest distance possible after collision. In result, we get minimum void space in the bed which results lowest value of the maximum fountain height. With the decrements of the value of e_{ss}, the collision becomes more inelastic; which means more mechanical energy dissipation. As a result more void space in the bed is created and we get higher value of maximum fountain height. Figure 2.3 (b) demonstrates the comparison results for different values of maximum packing limit $\alpha_{s,max}$. It confirms that there's no significant deviation of results due to the change of $\alpha_{s,max}$. With increasing $\alpha_{s,max}$, the maximum velocity slightly increase. The

reason behind this situation is the radial function g_0 is the function of $\alpha_{s,max}$ which is a correction factor that modifies the probability of collisions between particles; also interpreted as the non-dimensional distance between spheres. So, for higher value of $\alpha_{s,max}$, the value of g_0 increases; that raises the value of local solid pressure. So, with increased local solid pressure, particles move faster when the high velocity gas hit that region; as a result higher velocity of particles is observed.

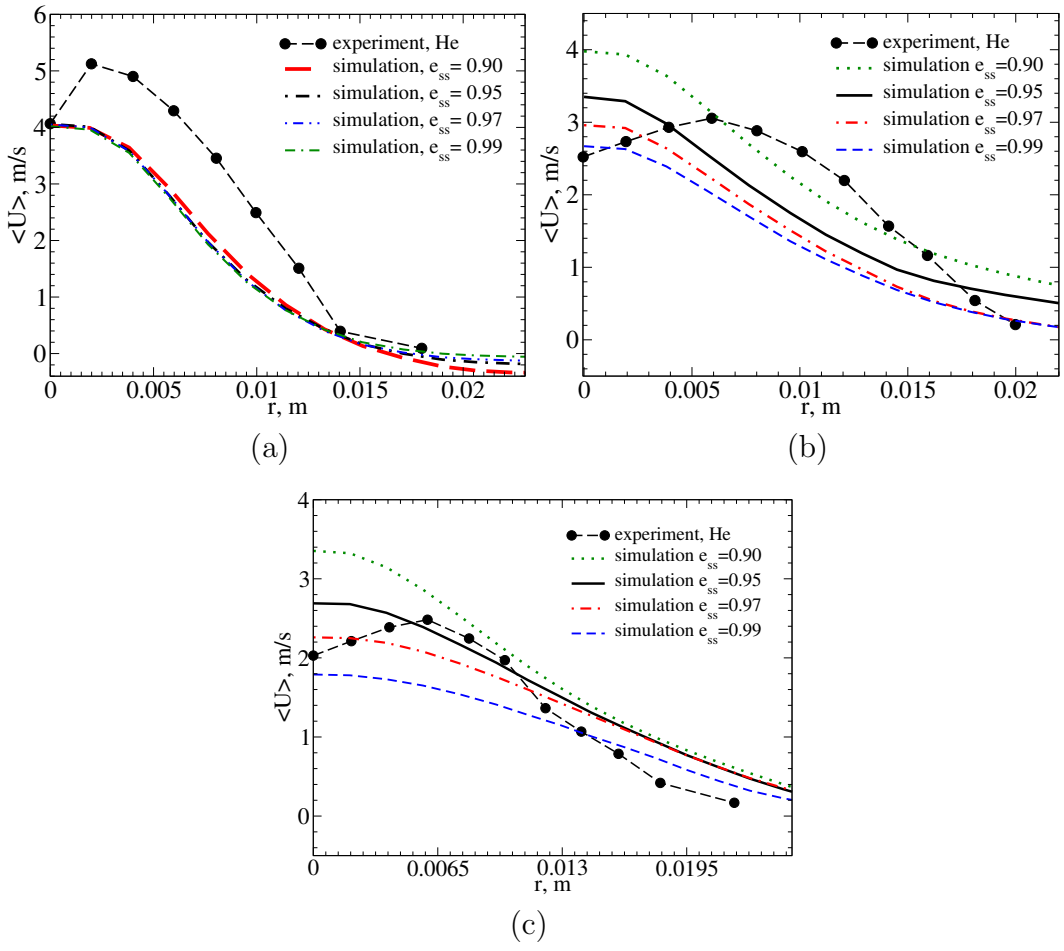

Figure 2.4: Radial profiles of the time-averaged velocity of the solid phase predicted using different values of the restitution coefficient where $\alpha_{s,max} = 0.61$ at (a) H=0.053 m (b) H=0.168m (c) H=0.268 m. Here 'experiment' data correspond to the work He et al.[2].

Radial profiles of vertical particle velocities in the spout of the column predicted for different e_{ss} and $\alpha_{s,max}$ are shown in Fig. 2.4 and 2.5. Figure 2.4 shows the radial profile in bed region whereas, figure 2.5 shows the radial profile in fountain region. It can be seen that simulation fail to predict correctly the particle velocity at the beginning of spout bed region, $z = 0.53$ m. At the same time, the results of our simulations are in good agreement with experimental data in the upper part of the spout, $z = 0.268$ m. Increase in e_{ss} from 0.9 to 0.99 leads to increase of the axial particle velocity. This effect is discussed later when transient dynamics of the bed is illustrated. From figure 2.4, we see the velocity of particles slowly increases to a maximum value with radial distance, then decreases consistently. A good agreement between experimental data can be seen with our simulation results for $e_{ss} = 0.90$ and $e_{ss} = 0.95$. They higher the restitution coefficient, the more the results are deviating from the experimental data. Figure 2.5 shows the radial profiles of the time-averaged velocity of the solid phase for different restitution coefficient at different height in fountain region. For every cases, we see simulation with $e_{ss} = 0.90$ predicted the results closer to the experimental data. For $e_{ss} = 0.95$, our simulation results match with experimental value for lower fountain height. For other restitution coefficient, we see much higher deviation from experimental results. Because as we explained before, the highest value of fountain height can be found for lower value of e_{ss}. For this reason, there is absence of fountain for higher value of fountain height which can be seen in our plot in figure 2.5 (b) and (c). Figure 2.6 presents voidage profile along radius of the spout bed for different height. We learn from here that for $e_{ss} = 0.90$ and $e_{ss} = 0.95$, the simulation results match with the experimental data better than the other values of restitution coefficient i. e. $e_{ss} = 0.97$ and $e_{ss} = 0.99$. Again, here we

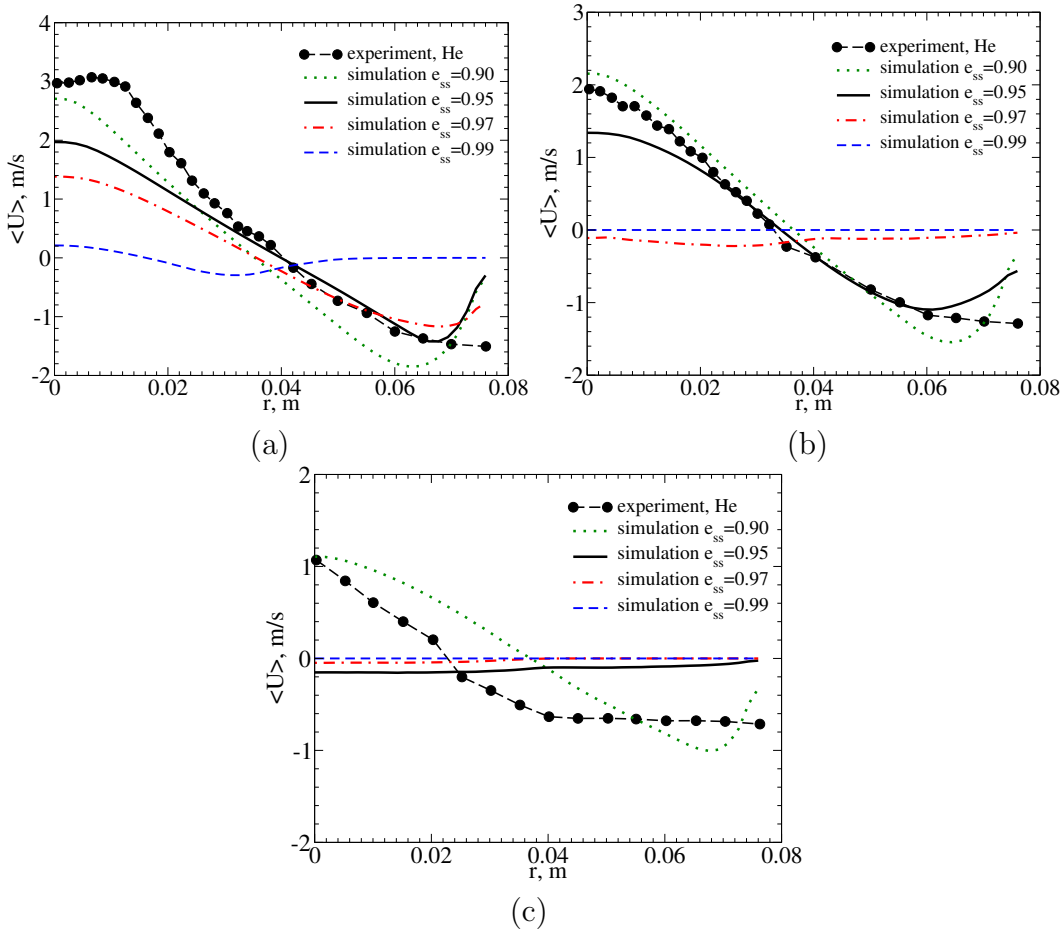

Figure 2.5: Radial profiles of the time-averaged velocity of the solid phase predicted using different values of the restitution coefficient at (a) fountain height = 0.045 m (b) fountain height = 0.145 m (c) fountain height = 0.295 m. Here 'experiment' data correspond to the work He et al.[2].

see that the lower value of e_{ss} increases the voidage. This is exactly the same scenario which was described in figure 2.3 that, with decrement of e_{ss}, the particle-particle collision becomes more inelastic. As a result, the particles are attached closer to each other; which makes more void space inside the bed and fountain; and thus, increases the voidage. From experimental data, voidage decreases with radial distance. but from simulation, voidage profile increases with radial distance a bit but after a certain value it reduces steadily. The

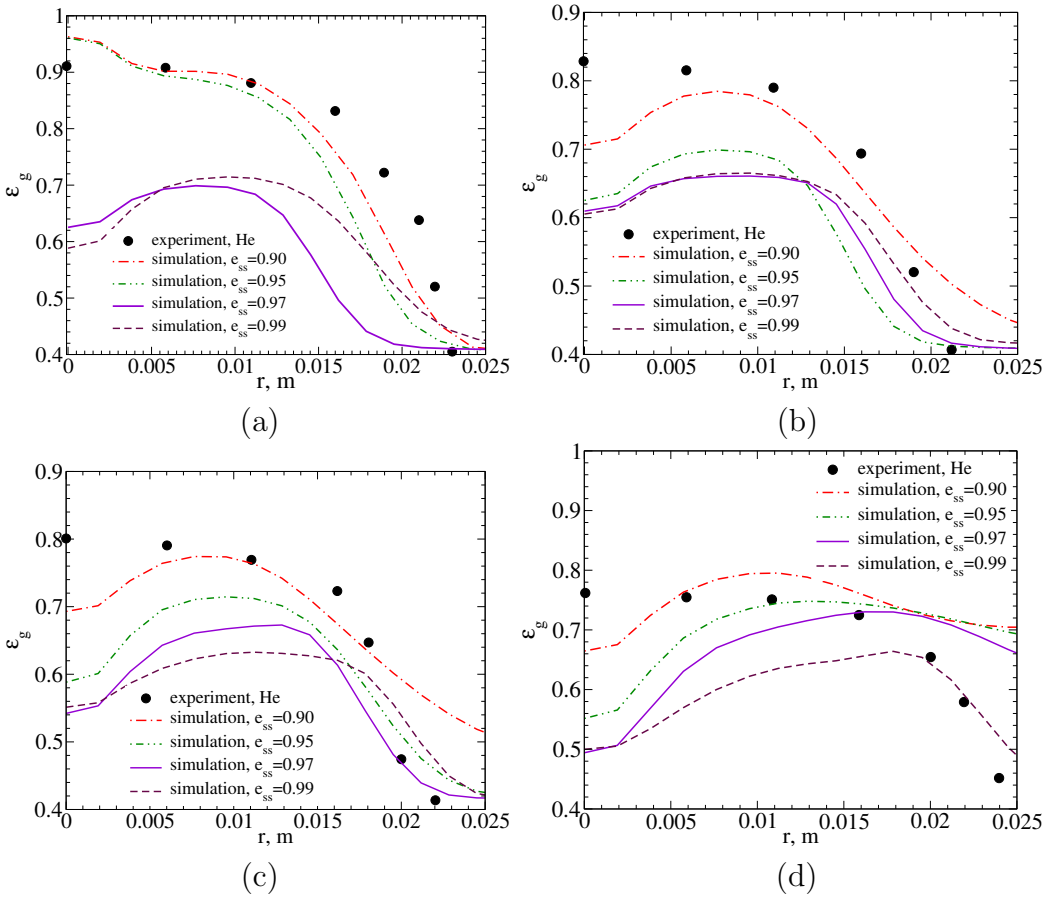

Figure 2.6: Voidage profiles of spout bed for (a) z= 0.053 m (b) z= 0.168 m (c) z=0.218 m and (d) z=0.268 m, using different values of restitution coefficient where $\alpha_{s,max} = 0.61$.

higher the height, the lower the maximum value of voidage.

Figure 2.7 shows the validation of our simulated spout profiles for different cases with the experiment. Spout profile means the boundary region between inlet gas and solid particles. Figure 2.7 (a) shows the effect of changing packing limit and figure 2.7 (b) shows the effect of changing restitution coefficient. From figure 2.7 (a) we see that spout profile height is increasing with the increment of $\alpha_{s,max}$. Because of increasing maximum packing limit, the solid pressure increases locally. As a result, when the particles start moving from a increased solid pressure region, they gain a higher velocity. On the other hand,

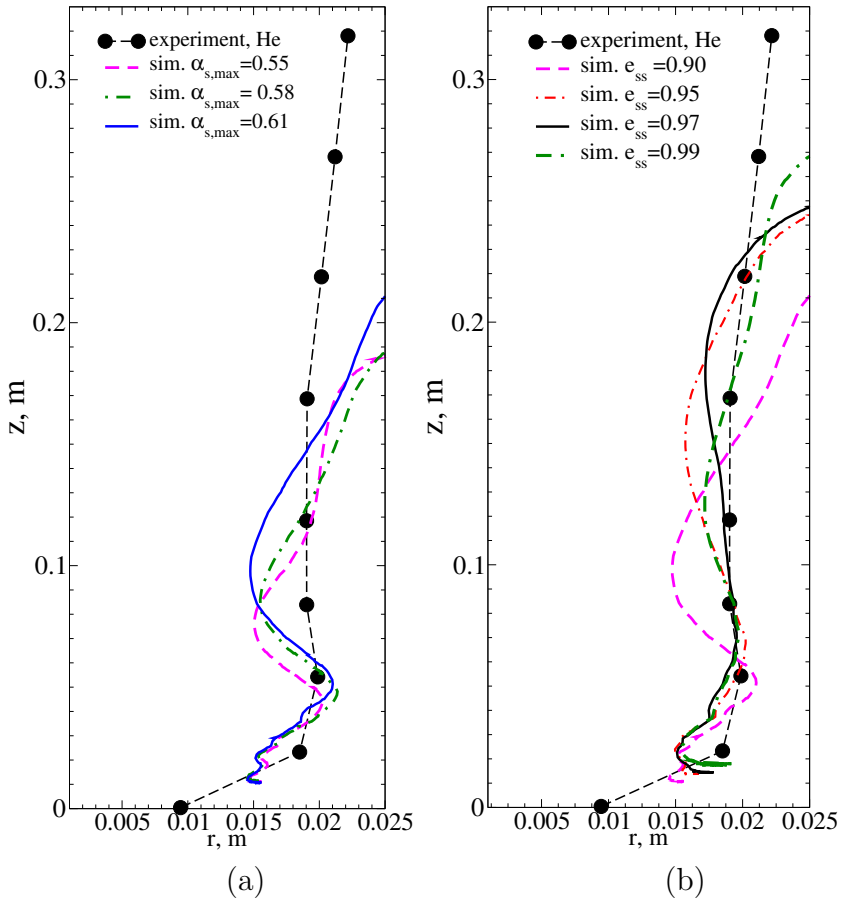

Figure 2.7: Spout profiles for (a) different packing limit with e_{ss}= 0.90 and for (b) different coefficient of restitution with $\alpha_{s,max} = 0.61$

in figure 2.7 (b) it can be seen that, all profiles have good agreement at the entrance region, where shape of the spout channel oscillates, see contour plots in figure 2.17 for more detail. In the middle section, restitution coefficient 0.9 gives more curve shape due to more unstable flow behavior. Due to higher velocity of solid phase we have more 'movable' solid bed in the down part of the spout bed reactor. We find here a good agreement of experiment and such kind of comparison was not shown in the work of Du et. al. [5]. Now we compare different drag models that has an important influence on the hydrodynamics of spouted bed. We compared axial profile of vertical particle velocity for

three different drag model i.e. Syamlal-O'Brein drag model [57], Gidaspow drag model [55], Wen and Yu drag model [56]. Our basic aim is to get a realistic spouted bed flow structure and test different gas-particle drag models. Figure 2.8 shows the comparison of axial profile of vertical particle velocity for

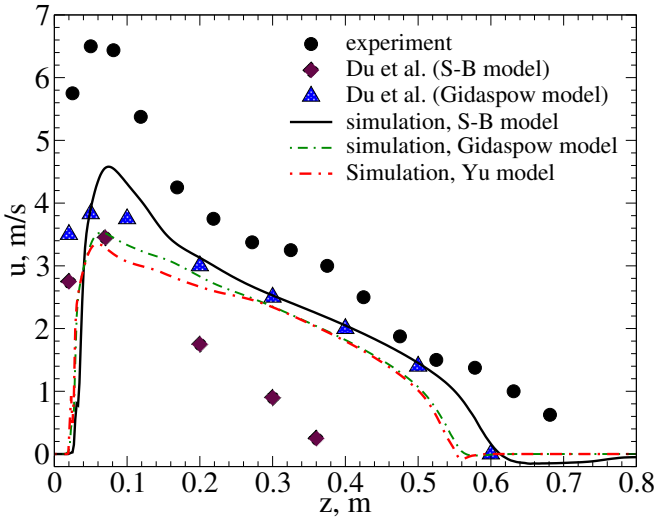

(a)

Figure 2.8: Comparison of axial profile of vertical velocity of particles for different drag model for $e_{ss} = 0.95$ and $\alpha_{s,max} = 0.61$

different drag models. We see here that, initially near to inlet region ($0 < z < 0.05$ m) all of the models are in good agreement with experiment, but they start deviating after 0.075 m. So, near to the region where ($0.1 < z < 0.2$), all of the models are differing from experimental data. Amongst them, Syamlal-O'Brein model give closer results to experiment. Time history of solid and gas phase can be seen in figure 2.9 for different drag models. In figure 2.9 (a), we see that gas phases are oscillating with higher amplitude for Syamlal-O'Brein model with a period of 1 second whereas, we get lower amplitude for other two. Wen-Yu model gives the lowest amplitude with lower oscillating period, while Gidaspow gives slightly higher value of amplitude and period. Figure

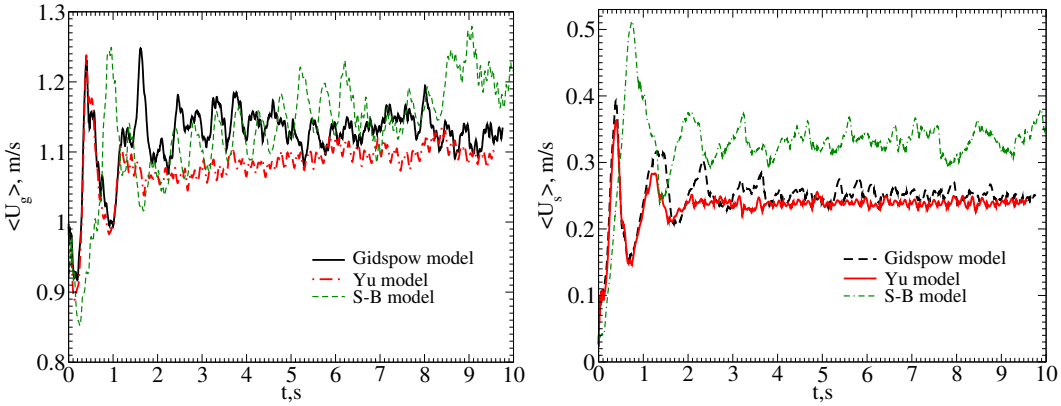

(a) (b)

Figure 2.9: Time history of (a) gas and (b) solid phase are shown for different drag model

2.9 (b) shows the time history of particle velocity. Here we see that particle flow is more unstable when Syamlal-O'Brein model is used. The start-up time for Syamlal-O'Brein is around 2 seconds wheres it reduces to 50% for other two models. The mean velocity reduces to 40% for Gidaspow and Yu model. Again, Syamlal O'Brien model gives larger amplitude of oscillation while Yu model gives the smallest amplitude of oscillation. Next, we are going to study the effect of initial packing to see how the behavior of spouted bed changes with it. Figure 2.10, 2.11, 2.12, and 2.13 shows the effect of change of different property with initial packing.

Figure 2.10 shows the comparison of time-averaged velocity of particles for different initial packing 0.61 and 0.58. Here, we see for lower value of initial packing, we get lower value of velocity profile. The reason of this scenario is for loosely packed bed, solid pressure decreases. So, when high velocity gas hits the particles, lower energy is transfer; in result we get lower value of velocity profile. Figure 2.11 shows the voidage profile along the radial direction at different height (H). We can see here that the voidage profile is

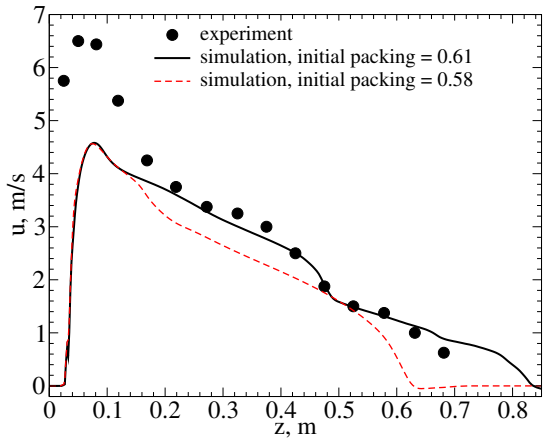

Figure 2.10: Axial profiles of the time-averaged velocity of solid phase predicted using different values of initial packing.

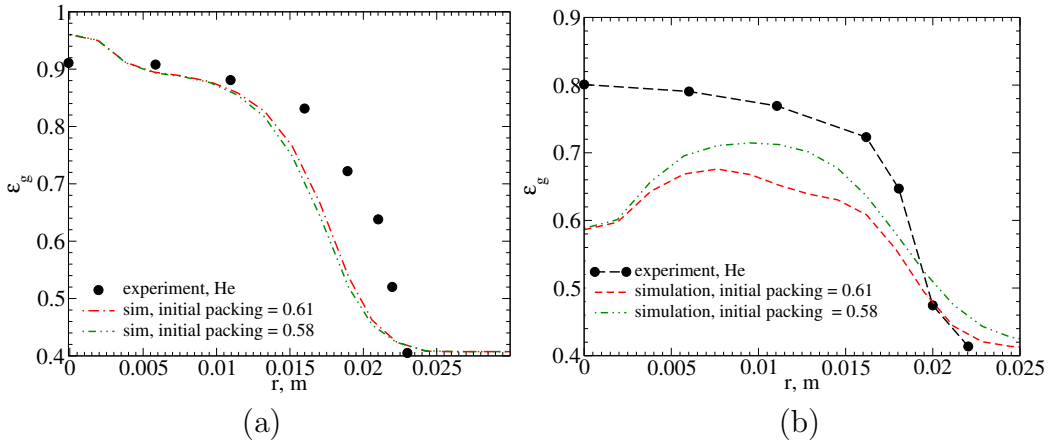

Figure 2.11: Voidage profiles predcited using different values of initial packing at (a) H = 0.053 m (b) H = 0.218 m

slightly changing with the change of initial packing. Logically, we should get a lower value of voidage for higher value of initial packing which we can also observe in our figure 2.11. For tightly packed bed, solid pressure increases; so, the kinetic energy required to move the particle is higher. When the gas with high velocity hits the bed, the particles moves with a higher potential resulting a larger void space between the particles. As a result, we get higher value of voidage. Figure 2.12 and 2.13 shows the radial profile of time-averaged velocity

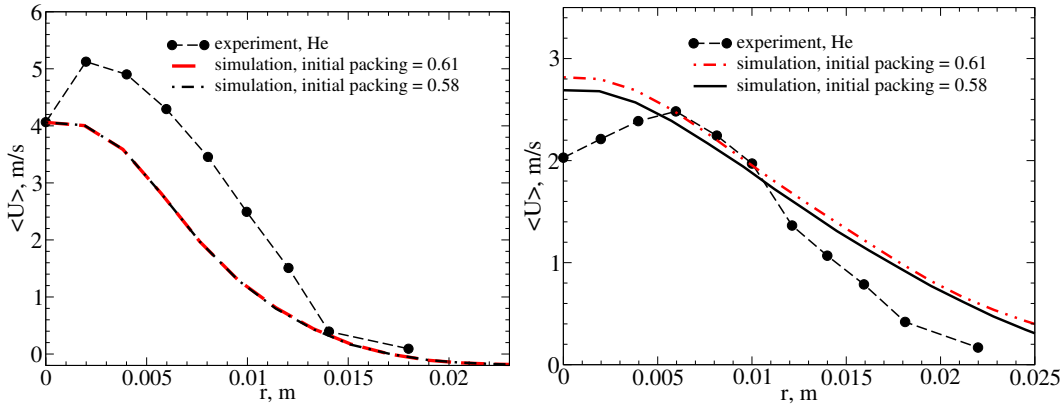

Figure 2.12: Radial profiles of the time-averaged velocity of the solid phase predcited using different values of initial packing at (a) H = 0.053 m (b) H = 0.268 m

of particles at different bed height. Figure 2.12 shows the radial profiles at bed region wheres 2.13 shows the radial profiles at fountain region. We see here the phenomena similar to figure 2.10. For higher value of initial packing, we get higher value of volume-averaged velocity. We already discussed the possible explanation of this phenomena in figure 2.10. For all of the figures, we see our model fails to predict radial profile initially, but then the profile starts to converge with the experimental value. Specially for fountain region, we get excellent agreement after 0.015 m.

Fig. 2.14 shows contour plots of the time average volume fraction of solid phase, α_s and the velocity magnitude $|u_s|$ of the solid phase predicted numerically using different values of the restitution coefficient e_{ss}. The analysis of this figure shown that decrease of e_{ss} leads to increase of fountain height. Detailed analysis of our results shows that this effect can be explained logically if we count that decrease in the restitution coefficient, e_{ss}, leads to the situation when inelastic collisions prevail.

From figure 2.14 it can also be seen that the simulation results changes

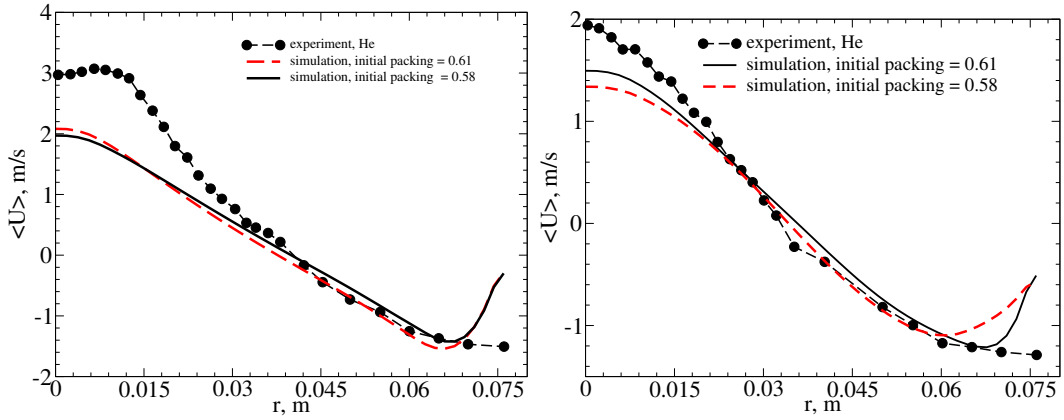

Figure 2.13: Radial profiles of the time-averaged velocity of the solid phase predicted using different values of initial packing at fountain height = 0.045 m.

rapidly due to the change of the values of e_{ss}. With higher e_{ss} value, we get slightly more stable fountain and lower fountain height. With lower values of e_{ss}, the collision of particles become more inelastic which provides more mechanical energy dissipation. For this reason, more particles compact in a small region and make more void space. As a result, for lower values of e_{ss}, we get higher fountain height. On the other hand, higher value of e_{ss} we get more elastic particle-particle collision; so particles moves to a higher distance from each other. Which makes lower voidage present in fountain and bed. Finally in result, we get lower fountain height.

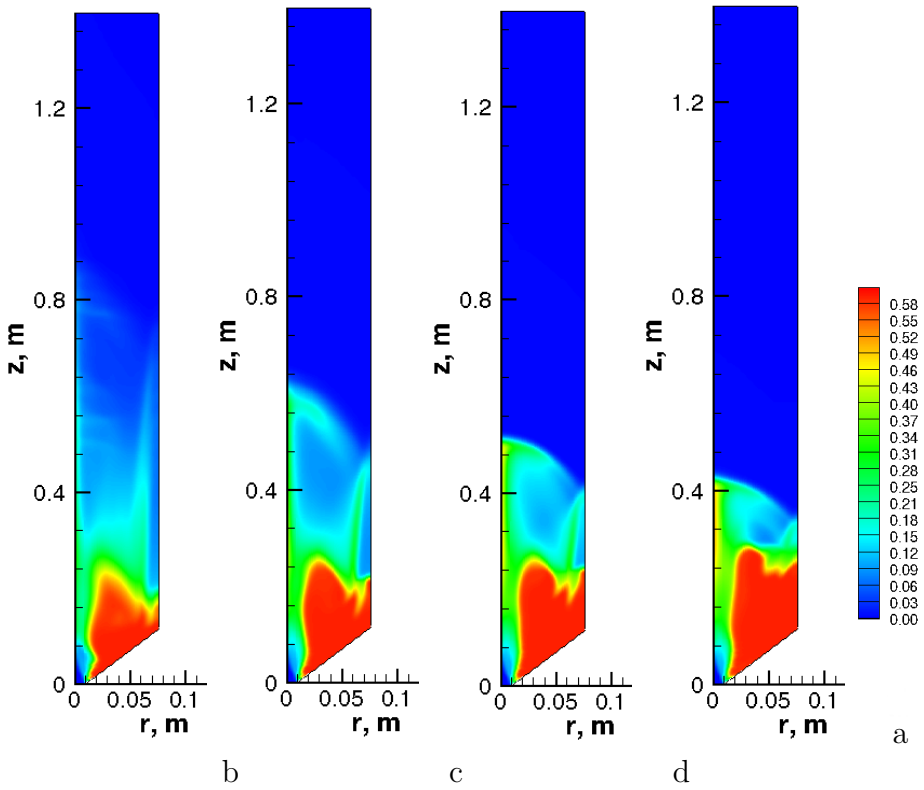

Figure 2.14: Contour plots of the time average volume fraction of solid phase, α_s - a)e_{ss}=.90 $\alpha_{s,max}$=.61 , b) e_{ss}=.95 $\alpha_{s,max}$=.61, c) e_{ss}=.97 $\alpha_{s,max}$=.61, d) e_{ss}=.99 $\alpha_{s,max}$=.61

Figure 2.15 shows the effect of maximum packing limit on spouted bed. From here we see that, there's no significant effect found on contour plots for maximum packing limit.

To study transient dynamics of the gas and solid flows in the spout bed we use so called volume-averaged or *global velocity* of the solid phase in the entire cavity. For this purpose we introduce the volume-averaged solid flow velocity U_l $(l = s, g)$:

$$U_{s,g} = \frac{2\pi}{V_{sb}} \int_0^R \int_0^H \left(\sqrt{u_{s,g,r}^2 + u_{s,g,z}^2} \right) r \, d\, r \, d\, z \tag{2.6}$$

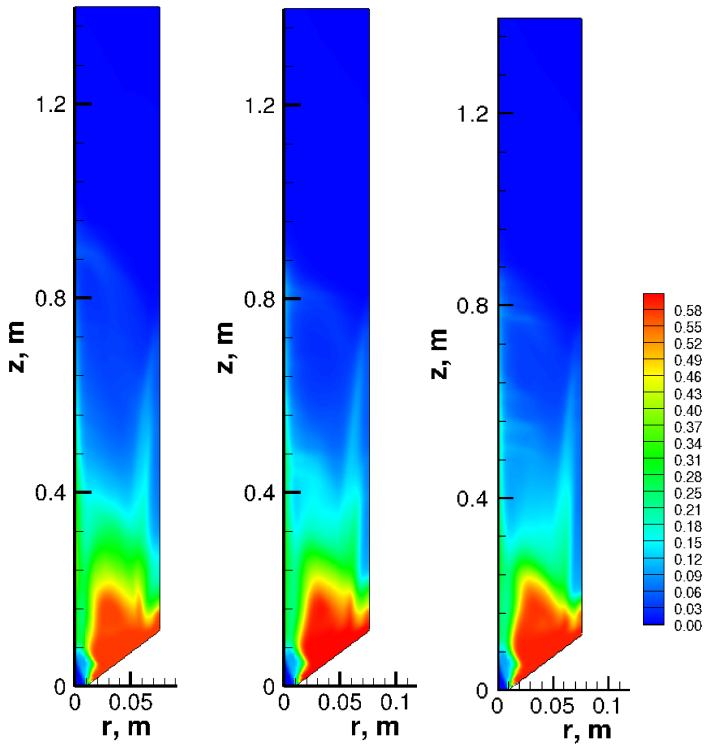

Figure 2.15: Contour plots of the time average volume fraction of solid phase, α_s - a)e_{ss}=.90 $\alpha_{s,max}$=.55 , b) e_{ss}=.90 $\alpha_{s,max}$=.58, c) e_{ss}=.90 $\alpha_{s,max}$=.61

where V_{sb} is the volume of the whole spout bed reactor, u_g and u_s are the velocities of the gas and solid phases.

Figure 2.16 shows the change time histories of volume-averaged velocity of solid and gas with different restitution of coefficient. We observe that the solid and gas volume-averaged velocity show periodic fluctuations. The higher the restitution coefficient, the lower the magnitude of fluctuation. Also we can see that, it takes 4-5 seconds to obtain developed unsteady regime. Usually the velocity magnitude gives a start-up kick to a higher value and suddenly decrease to a lower value and continue periodic fluctuations. For gas the magnitude of volume-averaged velocity and the period of oscillation is higher than the solid particle.

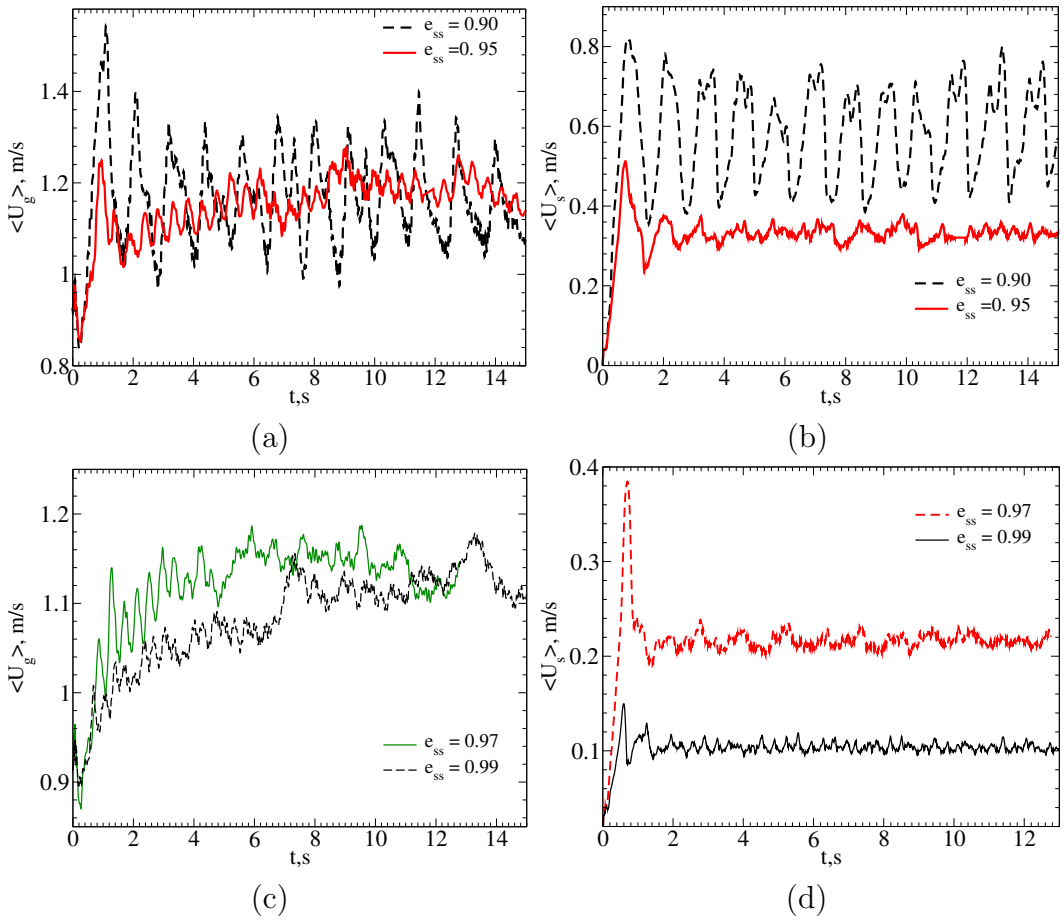

Figure 2.16: Time histories of the volume-averaged velocities of the gas and solid phases predicted numerically for different values of the restitution coefficient e_{ss} and for a fixed maximum packing limit, $\alpha_{s,max} = 0.61$

The time history of $U_{s,g}$ depicted in Fig. 2.16. shows that the initial start-up time is about of 2-3 sec. The developed unsteady regime is reached after 4-5 sec. It turns out that the decrease in the value of the restitution coefficient e_{ss} leads to the increase in the amplitude and in the period of oscillations of the volume-averaged velocity of the gas phase and solid phase. This effect is very good agreement with our explanation that decrease in e_{ss} produce more inelastic collisions and the particles attach more closer to each other creating more void space. Which increases the instability.

This effect is seen in Figure 2.17, which depict snapshots of the volume fraction of the solid phase, α_s, at different times corresponding to local maxim and minima in $U_{g,s}$ depicted in Fig. 2.16. First, the formations of *spout*, *fountain* and *annulus* are clearly seen in those snapshots. As expected, the spout channel is characterized by low values of the volume fraction of solid phase and high velocities of gas phase and particles.

The shape of the spout channel oscillates due to interplay between inlet gas and particles in the annulus zone, located between the spout channel and bed side-wall. Particle movement in the annulus region has toroidal clockwise direction. Instabilities in the inlet zone of the annulus lead to the large scale oscillations of the fountain, where particles coming from the spout channel rise to the top and fall back due to the gravity. During particles falling back they interact with next particles coming up from the spout channel leading to decrease of the fountain height. This effect causes the increase in the pressure inside the spout channel and after going increase in fountain velocity. And the whole cycle repeats again.

Figure 2.17 shows the flow patterns in spouted bed. In the spout zone, particle concentration is low and particle velocity is very high. So, the particles are carried away to upward direction by gas to the higher zone forming a fountain region. Here in fountain region, particle concentration is higher than the spout region and thus, the particles create pressure to the downward particles. But the downward particles with higher velocity, push the upper fountain particles and force those particles to move to the annulus region. As a result an oscillating motion appears with time. In the annulus region, we find the particle concentration is highest and the velocity of particles are lowest. The particles move to the axis of spouted bed in downward direction because

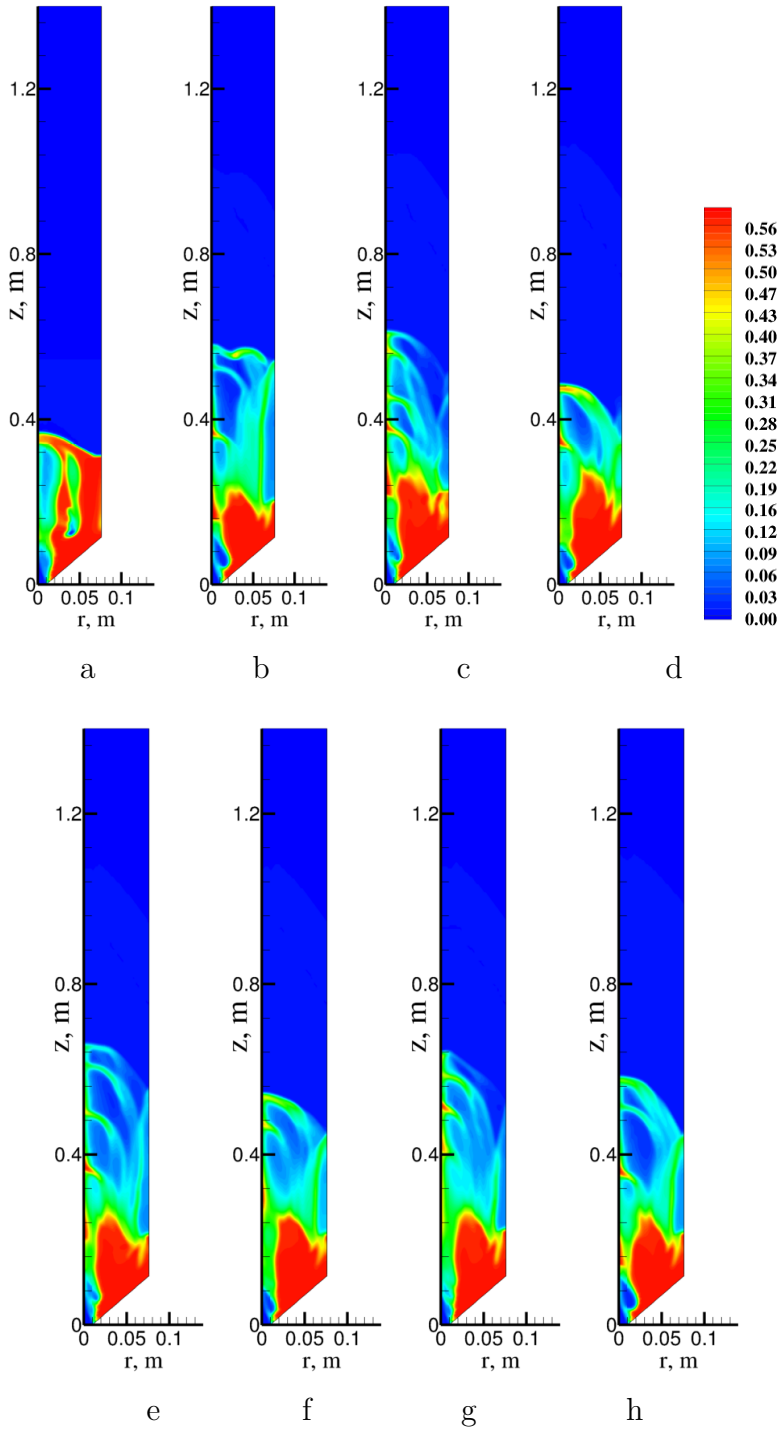

Figure 2.17: Snapshots of the volume fraction of the solid phase predicted numerically for the restitution coefficient of $e_{ss} = 0.95$ and packing limit $\alpha_{s,max} = 0.61$. Here different times corresponds to local maxima and minima in U_s depicted in Fig. 2.16: a) - 0.244 s, b) - 0.906 s, c) - 1.201 s, d) - 1.348 s, e) - 2.157 s, f) - 2.378 s, g) - 2.598 s, h) - 8.999 s.

of the lower concentration and higher velocity of particles in spout region.

Now, we study the effect of swirling velocity with inlet gas. We compare results with 'no swirling' simulations by showing axial profile of vertical particle velocities, radial profiles of vertical particle velocity and voidage, contour plots etc.

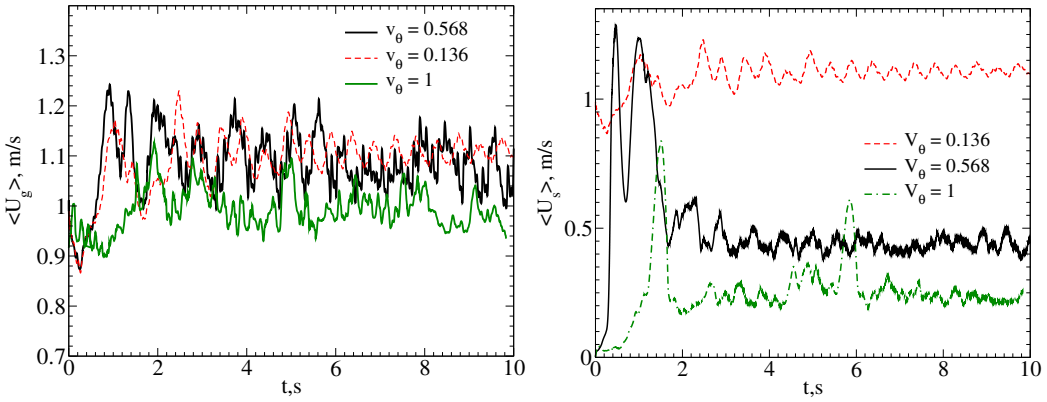

(a) (b)

Figure 2.18: Time history of (a) gas phase (b) solid phase for swirling

Figure 2.18 shows that the increase for the swirl velocity ratio leads to decrease the absolute value of solid velocity. So, additional swirl significantly decrease the absolute velocity of solids around 70% However at the same time the velocity of gas is slightly decreasing around 20% of value. Time history of global velocity shows that for the swirl ratio of 0.136 after 4 seconds we get periodic oscillation with period of 0.5 second. At the same time the increase of velocity ratio decreases the amplitude of particle oscillation. On the other hand, for the gas phase the amplitude is increased. To illustrate this phenomena we plot contour plot of volume fraction calculated for different swirl velocities.

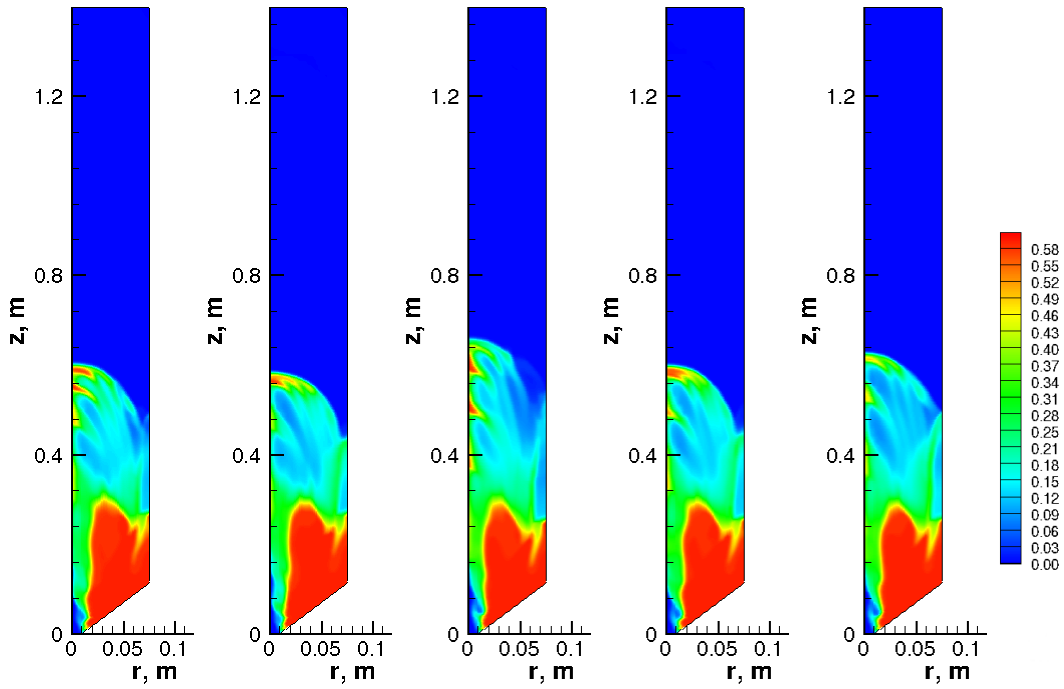

Figure 2.19: Contour plots of partical phase for swirling ratio = 0.136 for a) t= 2.81s b) 2.875s c) 3.74s d) 3.88s e) 7.345s

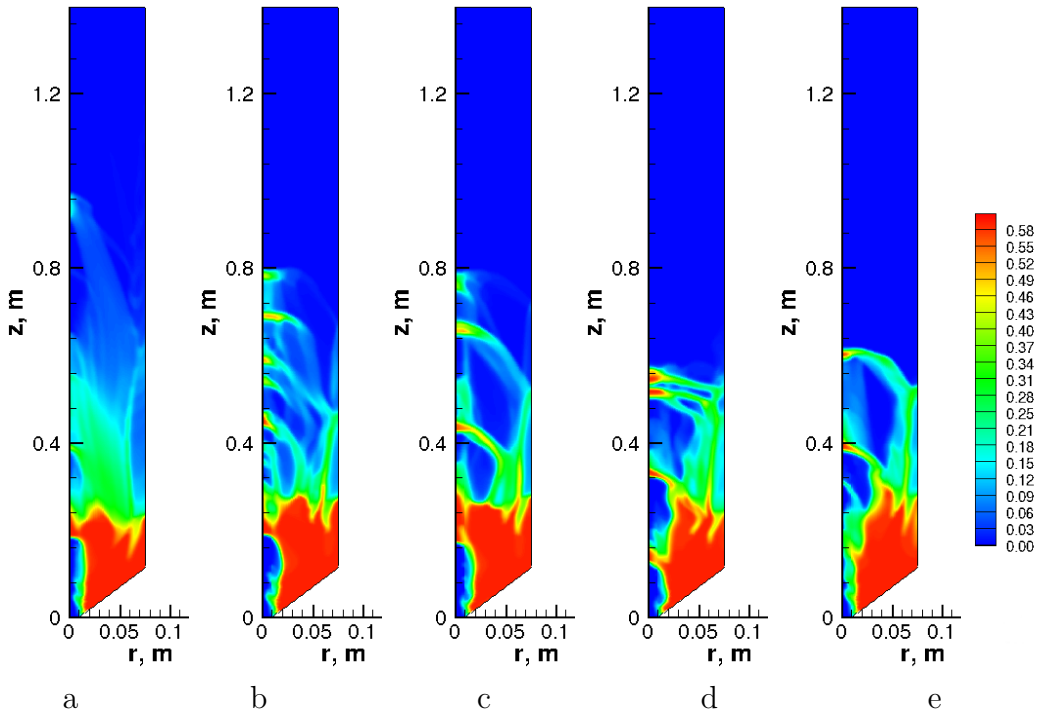

Figure 2.20: Contour plots of particle phase for swirl ratio of 0.57 at different time a) t= 1.02s b) t=1.675s c) t=2.675s d) t=2.875s e) t=10.0s

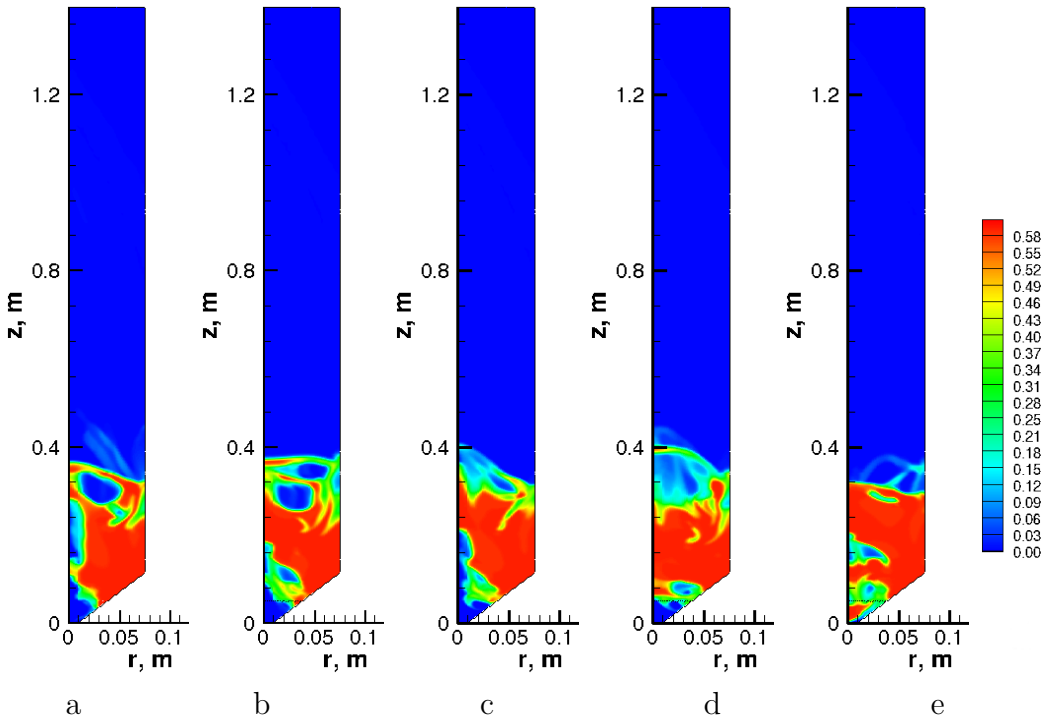

Figure 2.21: Contour plots of partical phase for swirl ratio of 1.0 at different time a) t= 1.506s b) t= 1.913s c) t=2.10s d) t=2.77s e) t=8.263s

Comparative analysis of these three pictures 2.19, 2.20, 2.21 shows that increasing swirl velocity $v_\theta = 1$ produce very small fountain while on the other hand for $v_\theta = 0.568$, we get highest fountain. For smaller swirling ratio v_θ =0.136, we get medium fountain with very good mixing of particles.

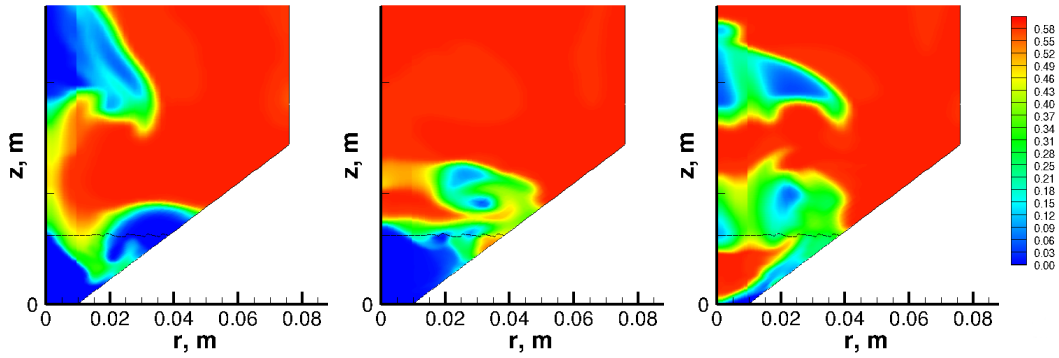

Figure 2.22: Zoomed view of contour plots of partical phase for swirling ratio of 1.0 a) t= 7.41s b) t= 8.003s c) t=8.263s

To better understand the phenomena of swirl velocity figure $v_\theta = 1$ 2.21, we plot figure 2.22 for further analysis. Here, we see that the inflow jet for the spout bed is destroyed by the higher velocity of swirl flow . Secondary flow caused by swirl modifies the inflow jet significantly. This effect is attributed to the Taylor-Goetler Vortices. Which can be identified in the above figures.

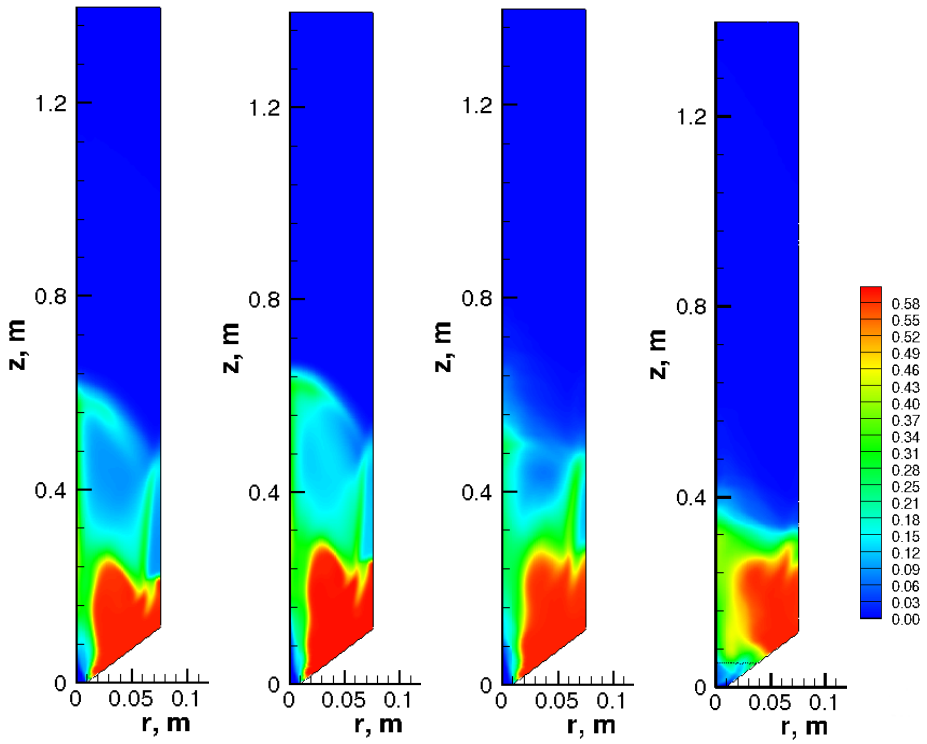

Figure 2.23: Contour plots of the time average volume fraction of solid phase, α_s - a) without swirl b) swirl ratio of 0.136 c) swirl ratio 0.57 d) swirl ratio of 1.0

Figure 2.23 shows the time average volume fraction of solid phase for 'no swirl' and for different values of swirl ratio. For lower swirl ratio, we get a higher fountain than 'no swirl' and the fountain is well spread; which indicates better mixing of particles. On the other hand for higher swirling ratio, the fountain becomes smaller and smaller; and for swirl ratio of 1.0, the fountain is almost touches the bed surface. Which can also be utilized in some industries.

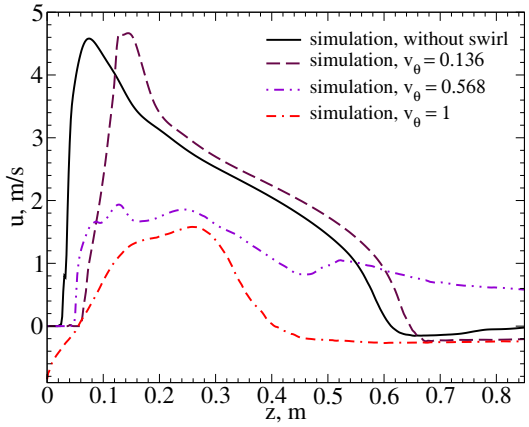

Figure 2.24: Axial profiles of the time-averaged velocity of the solid phase. Here 'simulation - without swirl' corresponds to the simulation work where $e_{ss} = 0.95$ and $\alpha_{s,max} = 0.61$

Figure 2.24 displays the axial velocity of solid phase along the axis of the spouted bed with and without swirl. For lower swirling velocity i. e. $v_\theta = 0.136$, we see that the maximum axial velocity and the velocity profile remain almost same but the profile shifts to right a little bit. Which means the increment of particle velocity along the axis starts from lower height. For larger number of swirling velocity i. e. $v_\theta = 0.568, 1$; maximum axial velocity of particle reduces.

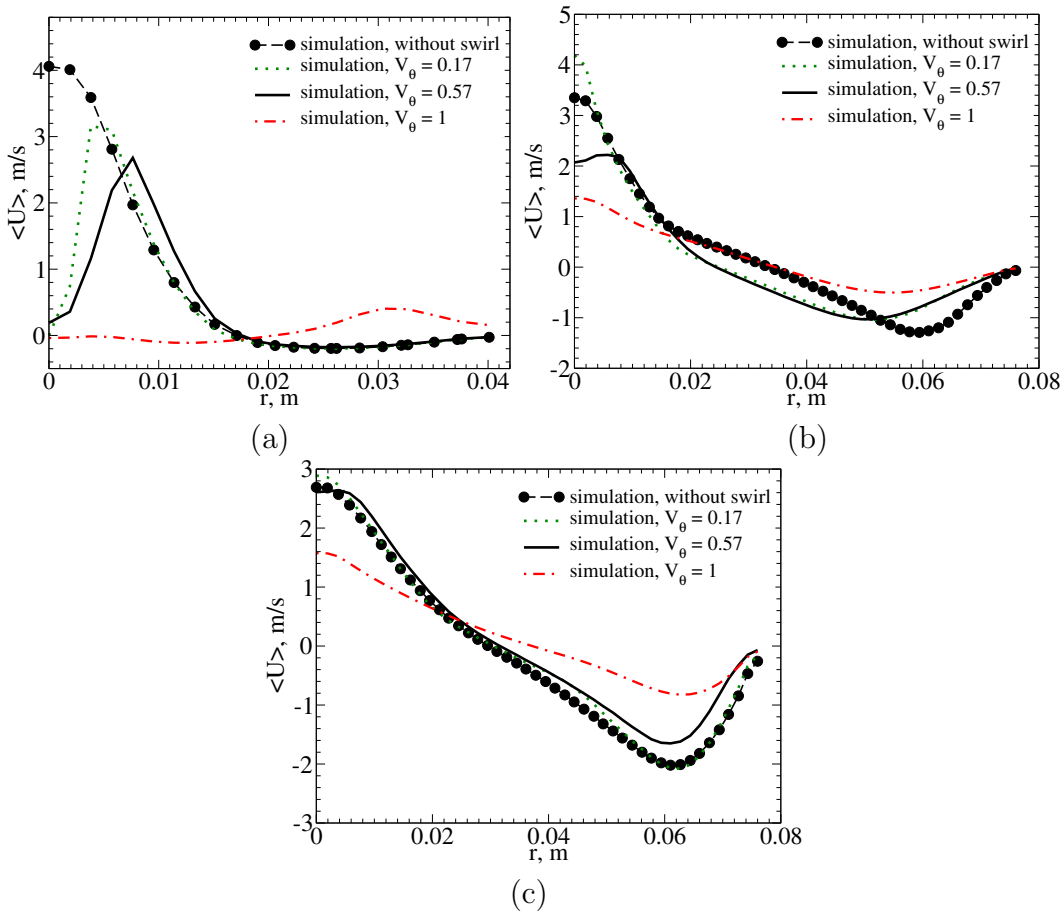

Figure 2.25: Radial profiles of the time-averaged velocity of the solid phase predcited using different values of swirl at (a) H=0.053 m. (b) H=0.168 m (c) H=0.268 m

Figure 2.25 shows the comparison of radial profiles of the time-averaged velocity of particles for different swirling velocity with simulation using no-swirl. For the lower value of height (H), we see here that the velocity is more deviating with swirl. When we take lower fountain height, the lower the swirling velocity the higher the maximum velocity we get along the radius.

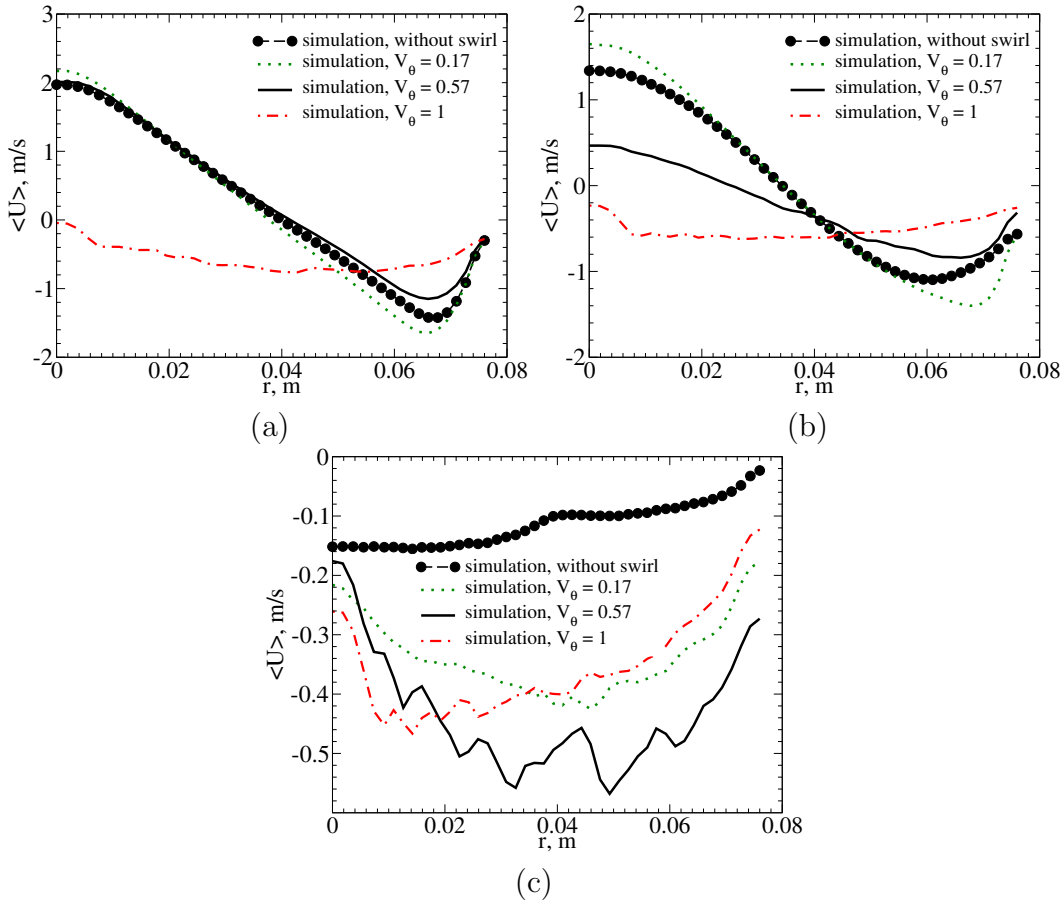

Figure 2.26: Radial profiles of the time-averaged velocity of the solid phase predcited using different values of swirl at (a) fountain height = 0.045 m (b) fountain height = 0.145 m (c) fountain height = 0.245 m

Figure 2.26 exhibits the comparison of radial profiles of the time-average velocity of particles for different swirling velocity with simulation using no-swirl in fountain region at different height. In this figure we can see that, for higher fountain height region, the velocity profile along radial direction is deviating with swirling velocity. Here we also see a periodic fluctuation of the velocity along the radial direction.

2.6 Summary

In this work we studied numerical the transient behaviour of particulate flows in a cylindrical-conical spouted bed, which was investigated in experimental work by He et al [1, 2]. he Euler-Euler unsteady multiphase laminar model with the *Syamlal-O'Brien* drag model available in commercial CFD software Fluent 14.0. was utilized. The results can be summarized as follows:

- The comparison of simulation results in the form of time-averaged vertical particle velocity against experimental data showed good agreement.
- The transient analysis showed that the start up time comprise of 2-3 seconds and the developed unsteady regime is reached after 4-5 seconds.
- Syamlal-O'Brein [49] drag model provided better agreement with experiment and presented more realistic behaviour of spouted bed than Gidaspow [55] and We-Yu model [56].
- The increment of restitution coefficient decreases fountain height and increases the elastic behaviour of the system. On the other hand, increment of maximum packing limit has negligible effect on the system.
- Lower swirling velocity ratio gives better mixing of particles with slightly higher fountain height where as higher swirling velocity ratio reduces spout height and introduce Taylor-Goetler vortices.

2.7 Future Recommendation

The list of future recommendation has been presented as follows:

- **Drag model:** One of the future recommendations can be optimizing drag model specific to spouted bed. We found that all of the drag models slightly under predict the maximum axial particle velocity. Optimizing drag model for spout bed may solve this issue.

- **Advanced turbulence model:** Advanced turbulent model LES (Large Eddy Simulation) can be tested to predict the behaviour of spouted bed. We have seen that, though the global Reynolds number for the system is low, but there is presence of instability at the inlet. More attention should be paid at that region.

- **3D modeling:** 3D modeling can be conducted to validate the axi-symmetric behaviour of the spouted bed.

Chapter 3

Numerical Modeling of Slurry Flows in A Rock Fracture

Next, we utilize Euler-Euler model described in Chapter 2 to simulate slurry (sand+water, 30% volume fraction of solid) flow in rock fracture. To validate this model we compare our model with Euler-Lagrange model.

3.1 Basics of Fracturing

Hydraulic fracturing is an important technology for stimulating wells to increase the rate of production of oil or gas. The main principle of hydraulic fracturing consists in pumping of a slurry into a cased wellbore at high pressure. Basically, a slurry is a viscous fluid and near-spherical particles (proppant or sand)[6]. During pumping this slurry flows into the reservoir through perforations in the casing causing some large planar fractures. It should be noted that the fluid pressure at the perforations has to be sufficiently high to overcome the least principal earth stress in the reservoir[58]. Finally, forced

movement of slurry along the fracture the fracture widens and propagates. When pumping ceases, most of the slurry fluid left in the fracture leaks off into the reservoir rock. At the same time the fracture walls are bordered and the the proppant left in the fracture after the fracture is closed. Finally, a narrow permeable channel (typically about 10 mm wide[6]) between the walls of the fracture (which can be several hundred meters long and is typically 50 to 100 m high[6]) is developed. As an example, Fig. 3.1 depicts a horizontal section of a typical fracture[6], where the red square indicates an area of modeling presented in this work. It should be noted that the propped fracture is much more permeable than the reservoir rock around it because the proppant particles are much larger than the grains of the rock. Details about the modeling and design of hydraulic fractures can be found in the book [58].

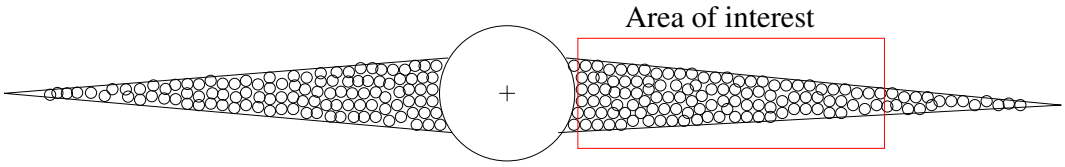

Figure 3.1: Schematic of a hydraulic fracture in a plane perpendicular to the well bore. Adopted from [6]. The red square indicates an area of modeling presented in this work.

3.2 State of Art of Modeling

As it was mentioned at the beginning hydraulic fracture can be defined as the process where hydraulic loading applied by a fluid inside a rock formation causes its fracturing. Applied to engineering science and technology hydraulic fracturing is extensively used in the petroleum industry for oil and gas recovery to maximize the extraction of inaccessible hydrocarbons. To understand the

processes during hydraulic fracturing and to optimize this technology many numerical simulations has been carried out covering three basic phenomena: the mechanical rock deformations induced by the fluid pressure, the flow of a mixture of viscous hydraulic fluid and sorted sand (proppant) within the fracture [59] - [60] and the fracture propagation [61].

Swadener et. al. [59] investigated hydraulic fracturing utilizing two-phase flow model. He injected water into the fracture which is saturated with oil at the beginning and then analyzed the growth of the fracture for a particular injection rate. His assumption includes 'uniform fracture', 'unidirectional permeating flow' and 'negligible capillary pressure'. He carried out the numerical investigation using iterative finite difference scheme and was able to analyze the hydraulic fracture growth successfully validating his numerical model with a single phase flow problem.

Ouyang et al. [62] carried out a numerical study using finite element scheme for proppant transport inside a hydraulic fracture. The numerical model utilizes 'governing equations for the propagation of a hydraulic fracture', 'the solution methodology in the GY-4M model of Gu and Yew [63]', 'conservation of mass', 'Fick's las of mass diffusion' and 'Shah's empirical equation' etc. to predict the phenomena accurately. He found a good quantitative agreement comparing the experimental data with an accurate 'fracture shape', 'fracture opening width' and 'borehole pressure' etc.

Adachi et al. [64] modeled the propagating hydraulic fracture by incompressible fluid in an in-permeable and linear elastic medium. The driving fluid was viscous with power-law rheology and a behavior index of greater than zero. He utilized 'elastic singular integral equation' and 'lubrication theory' to model this phenomena. He calculated different parameters such as 'crack

length', 'fracture opening', 'net fluid pressure' and 'fluid flow rate inside the crack' etc. He also studied the change of fluid index in the propagation of crack. In another work [65] Adachi et al. briefly discussed 'the computer simulation of hydraulic fractures'. He indicated different numerical simulation problem with modeling of hydraulic fracturing and described some of the mathematical techniques to get a better solution. At the end they addressed some of the key areas of research that is needed to be focused to improve current models for modeling of hydraulic fracturing.

It should be noted that up to date the flow of viscous fluid and proppant in fractures is basically modeled using analytical solutions of Simplified mathematical models [60] or by very simplified conservation equations, which do not reflect real physical processes occurring in a flow composed of a viscous fluid and solid particles. One of the challenging problem in modeling of hydraulic fracturing is a realistic prediction of a slurry flow, composed of a fracturing fluid and particles (So-called proppant), in a fracture. In particular, during the pumping sand slurry into the fracture the flow is affected by non-uniform distribution of sand particles due to hydrodynamics forces caused by wall-particle, particle-fluid and particle-particle interactions. These forces are responsible for segregation of sand in a rock fracture. Finally, possible segregations in grain locations may destroy gas/oil flows in deep rocks. In spite of the large number of numerical simulations on proppant motion in fracture up to date [65], the research in the area of proppant transport and possible segregation phenomena has been limited. One of the main reason of such a limitation is complexity of processes and lack of reliable models which can describe them adequately without complex mathematical assumptions. The present study undertakes computational study of the slurry flow behavior in a

rock fracture and possible transverse proppant segregation concentration using Euler-Euler-based approach. Special attention is paid to the consideration of non-Newtonian effects in the carrying fluid used in fracturing. An additional important consequence of this research work is that the newly developed numerical model and results of simulations can be used to validate a simplified engineering model used by Schlumberger at the field scale.

3.3 Model Formulation and Input Parameters

3.3.1 Problem Setup

Next we discuss our problem setup presented schematically in Fig. 3.2. In particular, it can be seen that we approximated a narrow permeable channel caused by fracturing, e.g. see Fig.3.1, by using a narrow rectangular channel with inlet, outlet and no-slip walls. In this work to study the propagation of slurry we use inflow velocity of particles 0.3 m/s with initial volume fraction of 0.3. In this work we use different geometries of the channel: one is straight channel and second case corresponds to *zikzak* shown in Fig. 3.3.2.

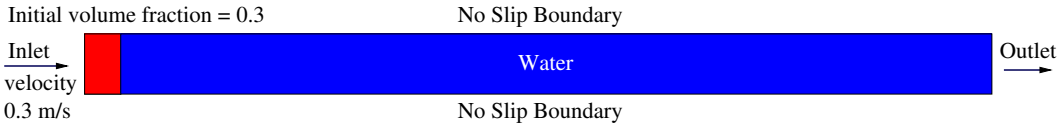

Figure 3.2: Scheme of setup including boundary conditions used for the modeling of for hydraulic fracturing.

3.3.2 Model

To model slurry propagation we utilize an Euler-Euler model for an unsteady laminar flow. The model description can be found in chapter 2. In particular, the Syamlal-O'Brein drag model is used for fluid-particle interaction. The list of model/ schemes are shown in table 2.2.

The corresponding input parameters used in simulations are listed below:

Figure 3.3.2 shows geometrical parameters for (a) straight shaped fracture

General Parameters	
particle diameter, d_p (mm)	0.6
particle density, ρ_s (kg/m^3)	999
Water density, ρ_g (kg/m^3)	999
Water viscosity (regular), μ_g (Pa/s)	$1.003 \cdot 10^3$
Inflow velocity, m/s	0.3
Inflow volume fraction of particles,	0.3
Straight shaped fracture	
Length (m)	1
Height (m)	0.01
$Reynolds_{particle}$	$=\frac{\rho_l \cdot u_{in} \cdot d_p}{\mu_l} = 179.28$
$Reynolds_{liquid}$	$\frac{\rho_l \cdot u_{in} \cdot D}{\mu_l} = 2988$
Zikzak shaped fracture	
Length (m)	5
Height (m)	0.01
Angle (m)	28.82^o
Viscous ratio = 5	
$Reynolds_{particle}$	$=\frac{\rho_l \cdot u_{in} \cdot d_p}{5 \cdot \mu_l} = 35.86$
$Reynolds_{liquid}$	$\frac{\rho_l \cdot u_{in} \cdot D}{5 \cdot \mu_l} = 597.6$
Viscous ratio = 30	
$Reynolds_{particle}$	$=\frac{\rho_l \cdot u_{in} \cdot d_p}{30 \cdot \mu_l} = 5.98$
$Reynolds_{liquid}$	$\frac{\rho_l \cdot u_{in} \cdot D}{30 \cdot \mu_l} = 99.6$

Table 3.1: Input parameters used to model slurry flow through hydraulic fracture.

and (b) zikzak shaped fracture. For straight shaped fracture we have length of 1m, but for the zikzak shaped fracture we have length of 5m with corner

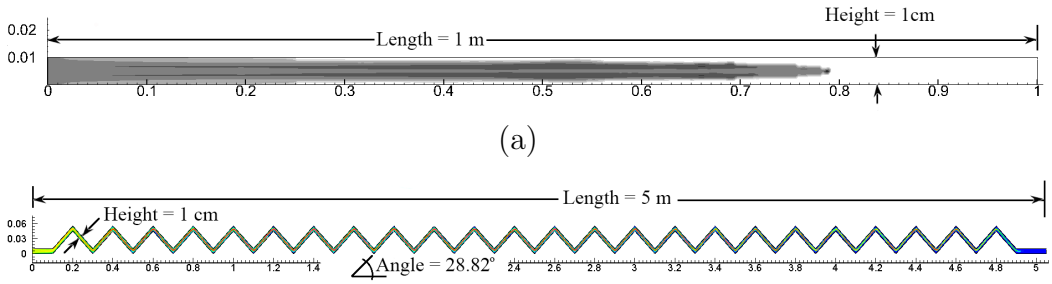

Figure 3.3: Scheme of geometry for (a) straight shaped fracture (b) zikzak shaped fracture

zikzak angle of 28.82^o.

Stokes number calculation:

Relation between the particle response time and the system response time is defined as Stokes number [7] page 497:

$$St = \frac{\tau_p}{t_s} \tag{3.1}$$

Where,

Particle response time, $\tau_p = \frac{\rho_p d_p^2}{18\mu_l} = \frac{999 \cdot \left(0.6 \cdot 10^{-3}\right)^2}{18 \cdot 1.003 \cdot 10^{-3}} = 0.01992$ sec

System response time, $t_s = \frac{L_s}{V_s} = \frac{D_{fracture}}{U_{in}} = \frac{1 \cdot 10^{-2}}{0.3} = 0.0333$ sec

Here,

L_s = Characteristic Length of the system

V_s = Velocity of system under investigation

So, Stokes Number, $St = \frac{0.01992}{0.0333} = 0.598$

3.3.3 List of Assumptions

Model assumptions for our course have been listed below:

- **Bulk liquid is Newtonian:** Our model assumes that the bulk liquid is Newtonian fluid.

- **Flow is laminar:** We calculate our Reynolds number for different cases. We found that the particle Reynolds number is very low. So, we assume our flow is laminar.

- **Restitution coefficient:** We assume that the coefficient of restitution for particle is 0.90.

- **Lift force and virtual mass force:** We assume that the lift force and virtual mass force in the system is neglegible.

3.3.4 Numerical Parameters

In this work, for every cases we utilize Euler-Euler multiphase flow model with Syamlal-O'Brein [49] drag law. Our time-step and maximum normalized residual varied with different geometry and dimension. In general, the minimum value of maximum normalized residual was kept below 10^{-04}.

For 2D straight shaped fracture, we use fracture length of 1m with 0.01m height. Inlet section comprises of 12 control volumes (CV) making a face area of $8.33^{-04}m^2$. Total number of control volumes were 14400 with control volume size of $6.94444^{-07}m^3$. The time step was set between 10^{-5} to 10^{-4}sec. Volume fraction equation for the gas phase was discretized in time using first-order implicit scheme. The number of iteration per one time step varied from 25 to 40, which guarantees the maximum normalized residual of about 10^{-4} for each time step.

On the other hand, for 2D zikzak shaped fracture, we have taken a frac-

ture with 5.02m long and a constant height of 0.01m. Similar to the straight fracture, the inlet section comprises of 12 control volumes. Total number of control volume was 72000 with control volume of size between $6.94444^{-07}m^3$ to $1.041667^{-06}m^3$. The time step was taken between 5^{-4} to 10^{-5} sec. The number of iteration per time step was between 15 to 30, which gave the maximum normalized residual of about 10^{-05} to 10^{-07}.

For 3D zikzak shaped fracture simulation, we take fracture with length of 0.8m, width of 0.03m and height of 0.055 m. Total number of control volume was 323664 and the rest of the configurations were similar to 2D zikzak shaped fracture simulation.

3.3.5 Model Validation

To validate our model we take compare results for ice particle sedimentation using Euler-Euler and Euler-Lagrange model[4]. It should be noted here that Euler-Lagrange simulations corresponds to 2D DNS simulations. The details on model formulation and numerical scheme can be found in the work[4]. The density of water was taken as 999.98 kg/m^3 and the density of ice particle was 916 kg/m^3. Figure 3.4 shows the validation of Euler-Lagrange model with Euler-Euler model for this slurry flow. For Euler-Lagrange model, we take 32 particles with radius of $0.2 \cdot 10^{-04}$ m. The number of control volume inside each particle is 16 and the size of control volume is $2.5 \cdot 10^{-05}m^3$ with e_{ss}=1.0. The grid resolution corresponds to 200 $\times$ 1000 CV in x and y directions, respectively.

On the other hand, for Euler-Euler model we use e_{ss} =0.95. Visually we see that both of the model show similar result and they both were able to form

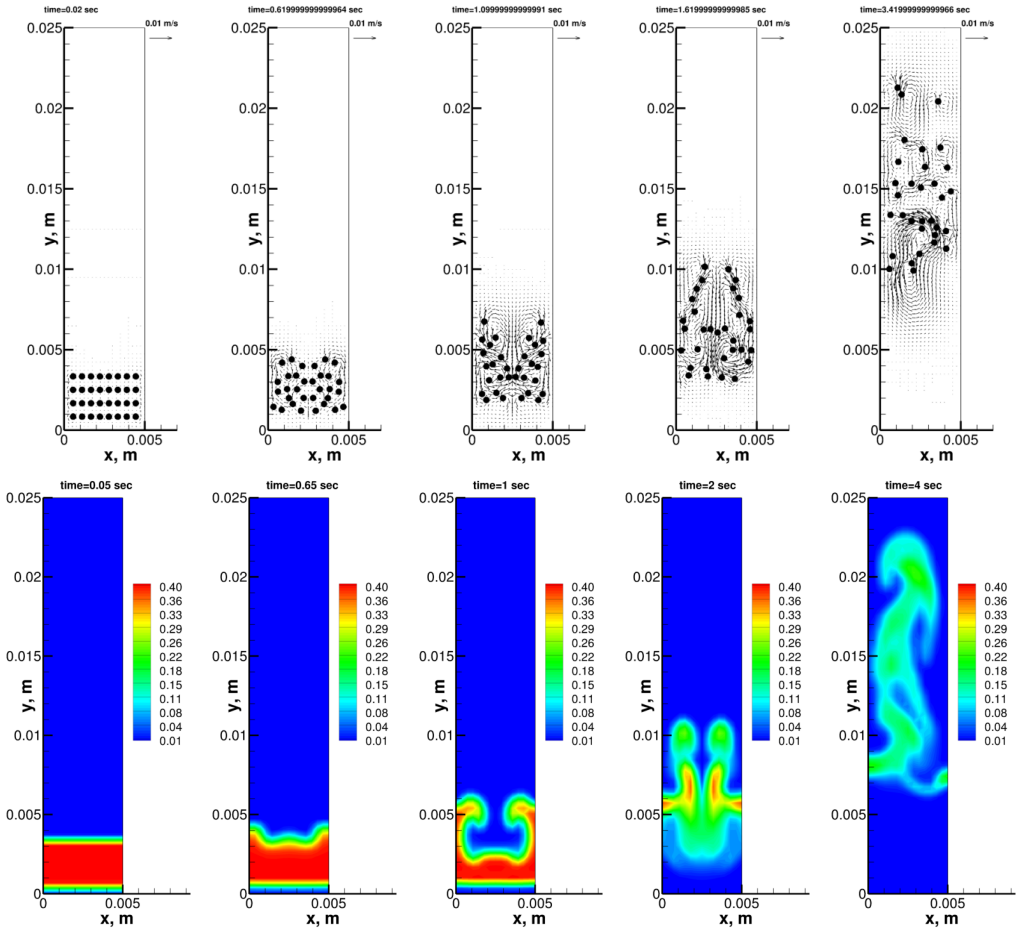

Figure 3.4: Snapshots of the volume fraction of particles predcited using different models: a) with Euler-Lagrange model at times (left to right) 0.02 sec, 0.62 sec, 1.09 sec, 1.62 sec, 3.42 sec; with Euler-Euler model at time (left to right) 0.05 sec, 0.55 sec, 1.0 sec, 2.0 sec 4.0 sec.

an *'M'* shaped front of the particles. It should be noted that the value of restitution coefficient (between 0.9 and 0.99) did not influence significantly the results. Finally, it can be seen that visual comparison of flow pattern predicted using Euler-Euler and Euler-Lagrange models shows acceptable agreement.

3.4 Results

We present our result for different configuration of fracture. First, we model our fracture assuming a straight shape. There we study different value of restitution coefficient. Then we model fracture using a zikzak shaped structure and we study transportation of slurry flow with different viscous ratio. In both cases, we also study the mixing zone. Finally, we study 3D zikzak shaped structure with different viscous ratio.

3.4.1 Straight Shape Structure

Fracture of Straight Shape with e_{ss} =0.90 .

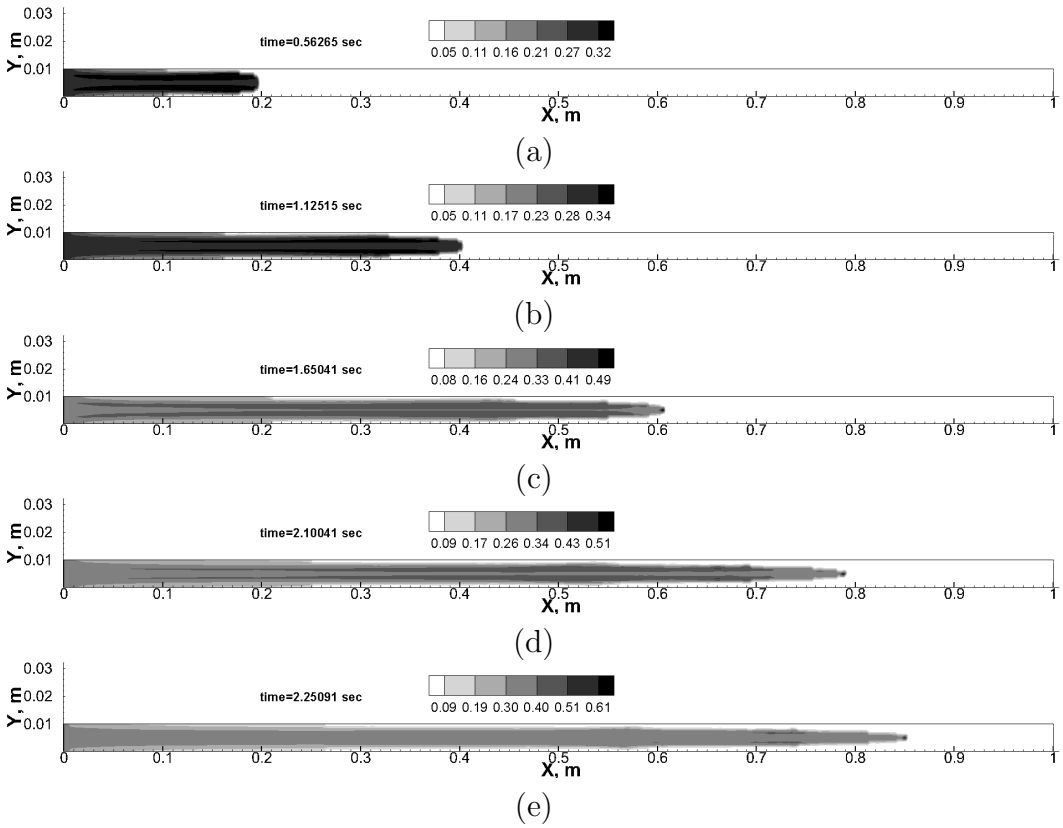

Figure 3.5: Contour plots of straight channel slurry flow with e_{ss} =0.90 at different time t = a) 0.56 sec b) 1.13 sec c) 1.65 sec d)2.10 sec e) 2.25 sec

From the figures 3.6 we see the propagation of slurry flow at axial direction. An interesting phenomena can be seen here that the maximum volume fraction of particles is increasing with time and at t=2.25 sec it reaches to the maximum number of 0.58. The slurry flows with a parabolic front carrying maximum volume fraction at the tip. Here, it is also to be noticed that the length of mixing zone is increasing with time and the parabolic profile of the front also becomes sharper with time. To understand these phenomena better, we plot volume fraction of particles in radial and axial direction as shown in figure 3.6

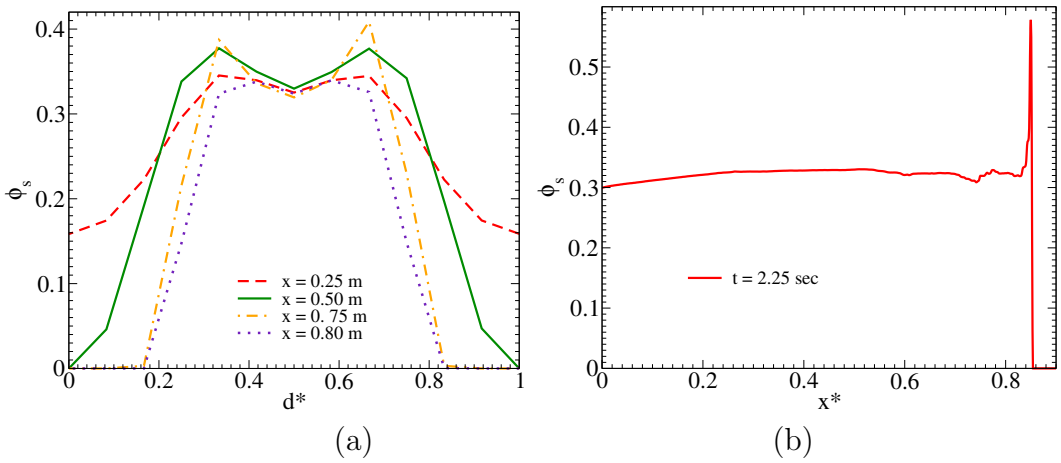

(a) (b)

Figure 3.6: Volume fraction of particles at time t= 2.25 sec a) in radial direction at different axial location b) in axial direction at centre line

Figure 3.6 (a) shows radial profiles of volume fraction at four location of the channel at t= 2.25 sec. We can see here an almost symmetric profile with the shape of an "M". Initially the "M" shape was wide spread and with the increment of length this shape is squeezed to a narrow shape of "M". It is also noticeable that the height of "M" is also increasing with length but decreased just before the tip. Which indicates that the front side contains more particles than the back side of the channel. From figure 3.6 (b) we see that the volume fraction suddenly increases to 0.58 at the tip of the front.

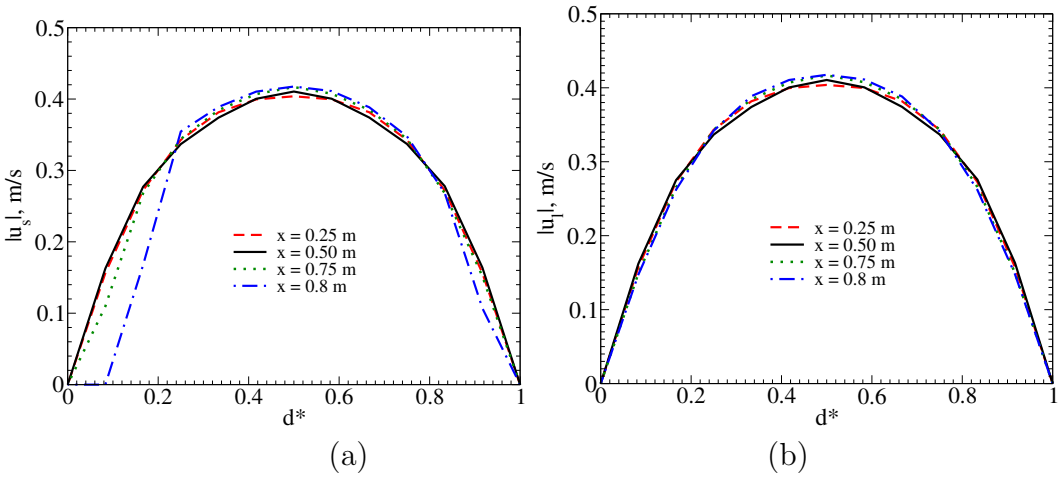

Figure 3.7: Velocity of a) particle and b) water in the radial direction at different axial location

Figure 3.7 shows that the velocity profiles for particle and water follows a parabolic curve and remains almost constant at different axial location. For particle velocity profile, we see zero velocity neat to the front because of the mixing zone. In the mixing zone, particles are absent near to the wall and as a result we get 'zero' velocity in that region.

Fracture of Straight Shape with e_{ss} =0.97 .

From the contour plot of slurry flow inside straight channel for $e_{ss} = 0.97$ depicted in figure 3.8, we see similar phenomena like $e_{ss} = 0.90$. Mixing zone, "M" shaped volume fraction profile, parabolic front everything is present there. But we can compare that for higher restitution coefficient (e_{ss}), the instability occurs sooner. Which means the volume fraction of tip reaches to it's maximum limit of 0.61 and then it starts showing instability.

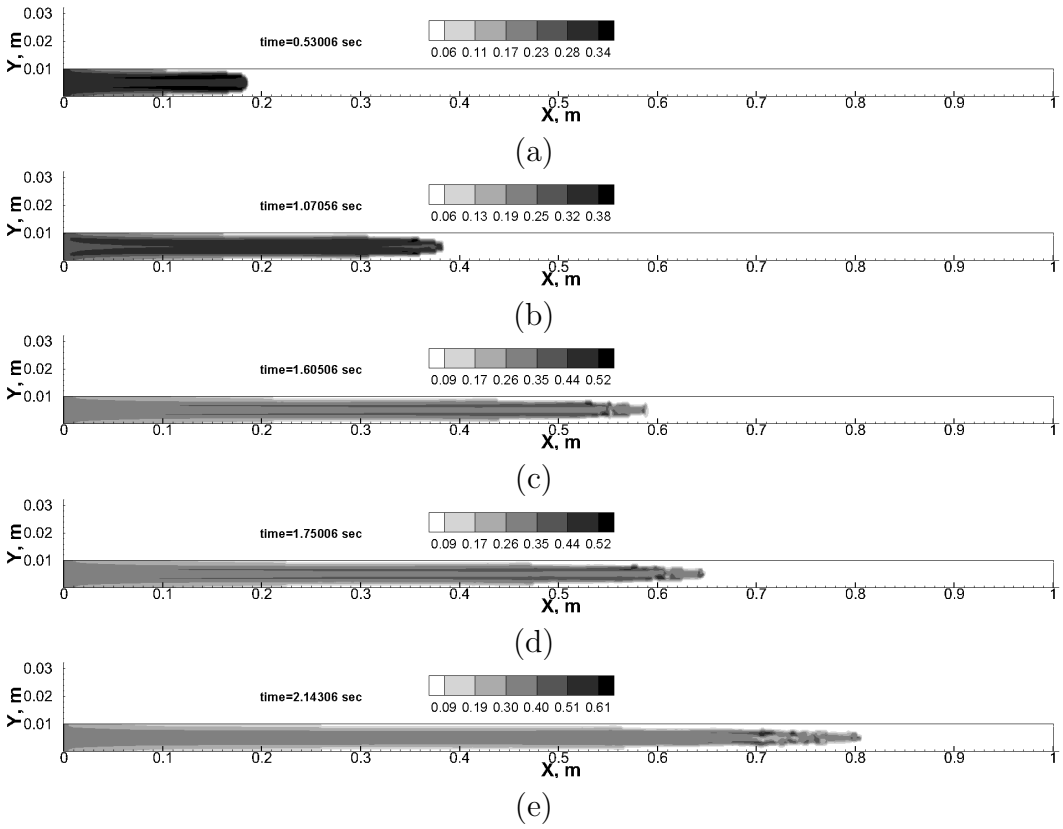

Figure 3.8: Contour plots of straight channel slurry flow with $e_{ss} = 0.97$ at different time t = a) 0.53 sec b) 1.07 sec c) 1.60 sec d) 1.75 sec e) 2.14 sec

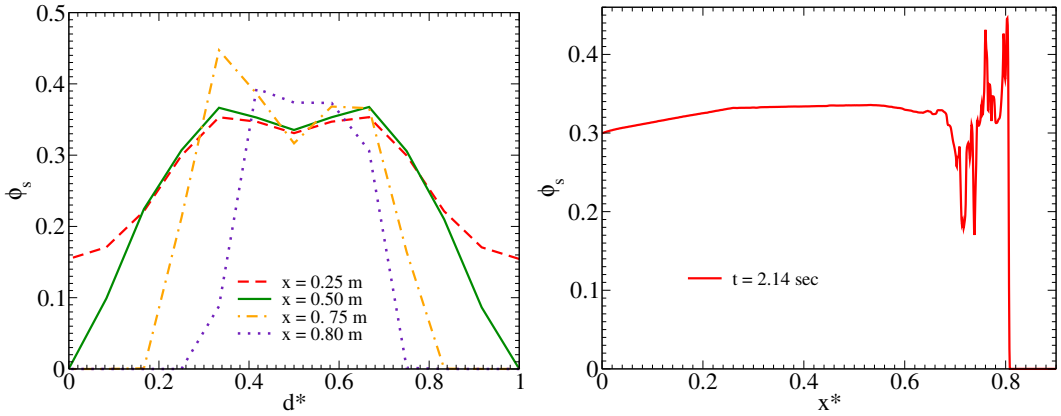

Figure 3.9: Volume fraction of particles for e_{ss} at time t= 2.14 sec a) in radial direction at different axial location b) in axial direction at center line

To better understand the phenomena of instability, we plot figure 3.9 to show the volume fraction of particles at different axial and radial location. We see that for figure 3.9 (a). the symmetric "M" shape becomes more asymmetric near to the tip region. And there is a maximum and minimum point of volume fraction present there. Figure 3.9 (b) shows the oscillation due to instability at tip. Figure 3.10 shows the velocity of particles and water along radial direction.

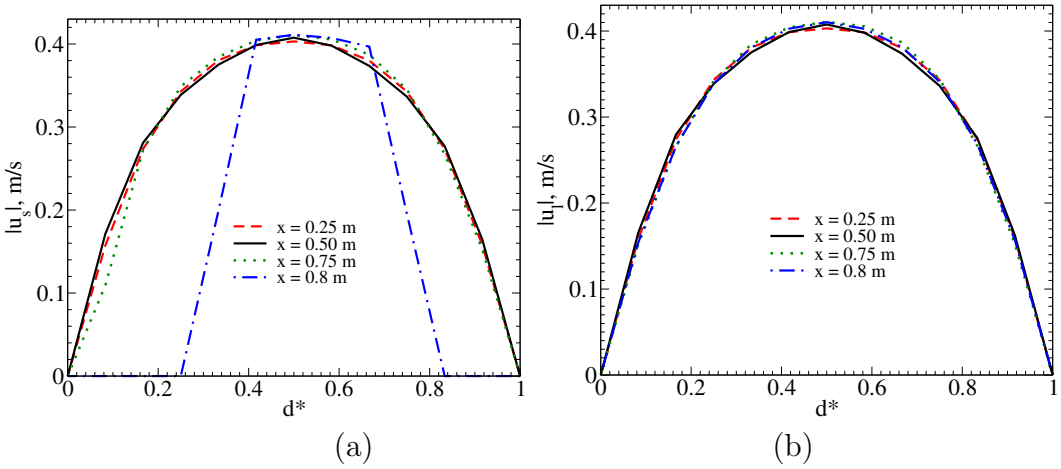

Figure 3.10: Velocity of a) particle and b) water in the radial direction at different axial location

It also forms a parabolic shape but the shape is deformed and cut-off from two sides near to the wall region close to the tip.

3.4.2 Fracture of Zizak Shaped Structure

Fracture of Zizak Shape with regularly viscous fluid .

Figure 3.11 shows the contour plot of volume fraction of particles at different time. We see that, there is no "M" shape front is present in this case. The reason behind this phenomena can be the zikzak shape of the channel. Here we also see the presence of 'mixing zone' where there is no particle near to the wall for a long region. This is possible because when particle front moves froward with a very low velocity, there's thin layer of water trapped inside the corner of the zikzak channel and it changes the direction of the slurry front from 'upward' to 'downward' and vise-versa. This is how the parabolic front shape of the slurry particles remain unharmed.

Figure 3.12 shows the volume fraction of particles at two different time in different locations. Here, we see a very interesting phenomena that initially at the beginning of the zikzak channel, there was a small straight portion where the "M" shaped front was initiated. But, with time the "M" shaped profile is destroyed and reformed to a "parabolic" curve. For a particular instance, the maximum point of the parabolic profile is decreasing. Which means the volume fraction at the tip is lower and the volume fraction at the beginning is higher. The reason behind the destruction of "M" shaped profile can be because of changing direction of the channel. When the slurry particles reaches to a changing point, the water layer trapped inside the corner pushes the particles to the center of the channel and make the "M" shape profile to

change into a “parabolic” curve.

Fracture of Zizak Shaped Structure With Viscous Ratio of 5 .

Figure 3.13 shows the contour plot for viscous ratio of 5.0 of zikzak channel. The phenomena is quite similar to viscous ratio of 1.0, but the difference we see here with the maximum volume fraction and mixing length. We see here that the maximum volume fraction has reduces to around 35%, where the length of mixing zone has been reduces to 50%. Here we also see the propagation of mixing length and a ‘parabolic’ front.

Figure 3.14 shows the volume fraction of particles at a) t =0.5 sec and b) t=11.50 sec in different locations. We also see a “M” shaped curve forming at the beginning of the channel initially, but again that is disturbed and reformed to a ‘parabolic’ shape. We also see the height of the ‘M’ shape is reduced to 80% and the maximum point for ‘parabolic’ curve has reduces to 35%. Similarly, the front contains lower volume fraction than the beginning of the channel and the height of the ‘parabola’ is increasing with length for a particular time.

Fracture of Zizak Shaped Structure With Viscous Ratio of 30 .

Again, we find similarity of our analysis for the contour plot of viscous ratio of 30. Figure 3.15 indicates the decrement of maximum volume fraction of the slurry flow. Mixing zone and parabolic front is also present here. Another interesting finding is the total travel distance of the particles for a specific time (say, t = 11.50 sec) is slightly increasing with the increment of viscous ratio. The decrement of maximum volume fraction is only 10% though the viscous ratio is increased significantly than the viscous ratio of 5.

Figure 3.16 shows the volume fraction of particles for a) t =.50 sec and b) t

= 11.50 sec at different location. Though we see “M” shape at the beginning, but it’s not properly developed and the maximum height of ‘M’ is also reduced rapidly 90% than the maximum height found for viscous ratio of 5.0. We also see the parabolic front of in figure 3.16 (b) showing the reduction of height for the parabolic curve with the increment of length.

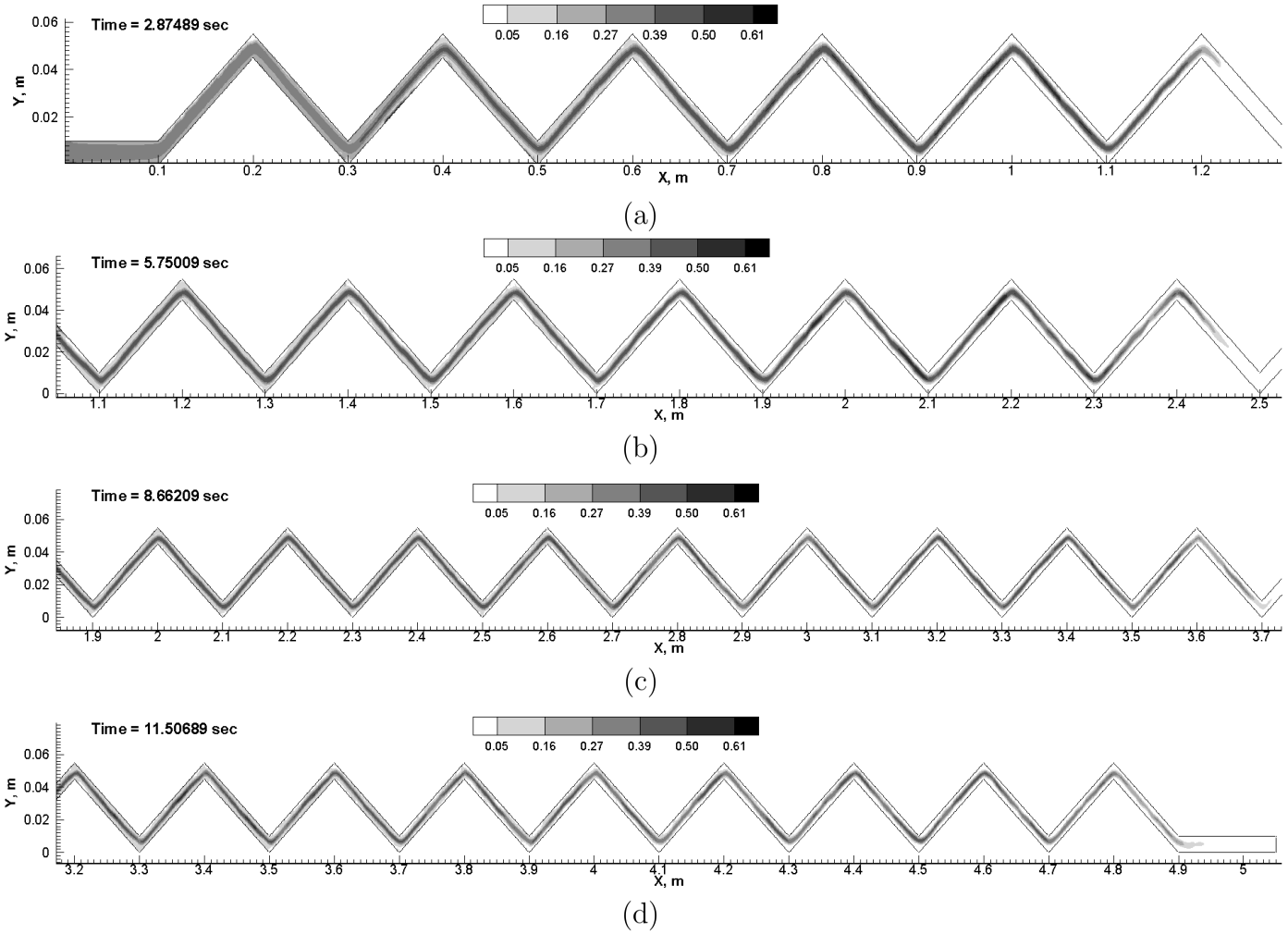

Figure 3.11: Contour plots of zikzak channel with viscous ratio of 1.0 for slurry flow with $e_{ss} = 0.90$ at different time t = a) 2.87 sec b) 5.75 sec c) 8.66 sec d)11.50 sec

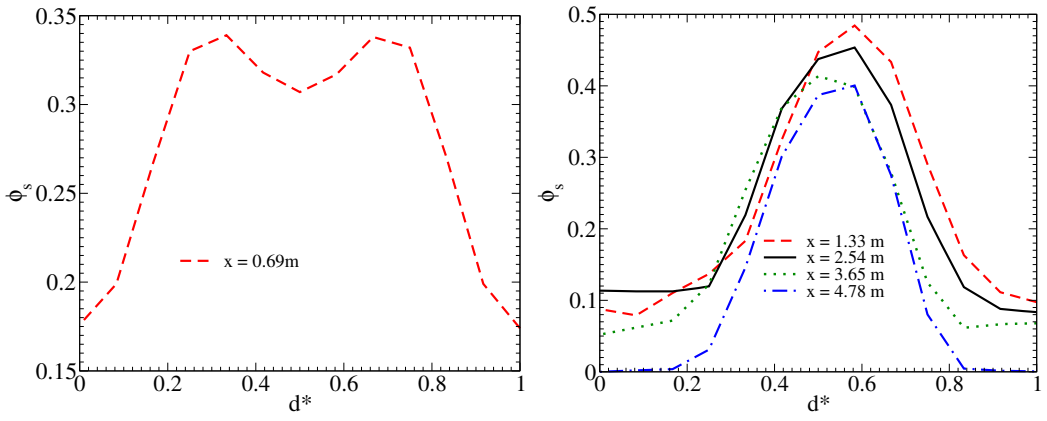

Figure 3.12: Volume fraction of particles for e_{ss}=0.90 at time a) t=0.5 sec b) t= 11.50 sec in radial direction at different axial location

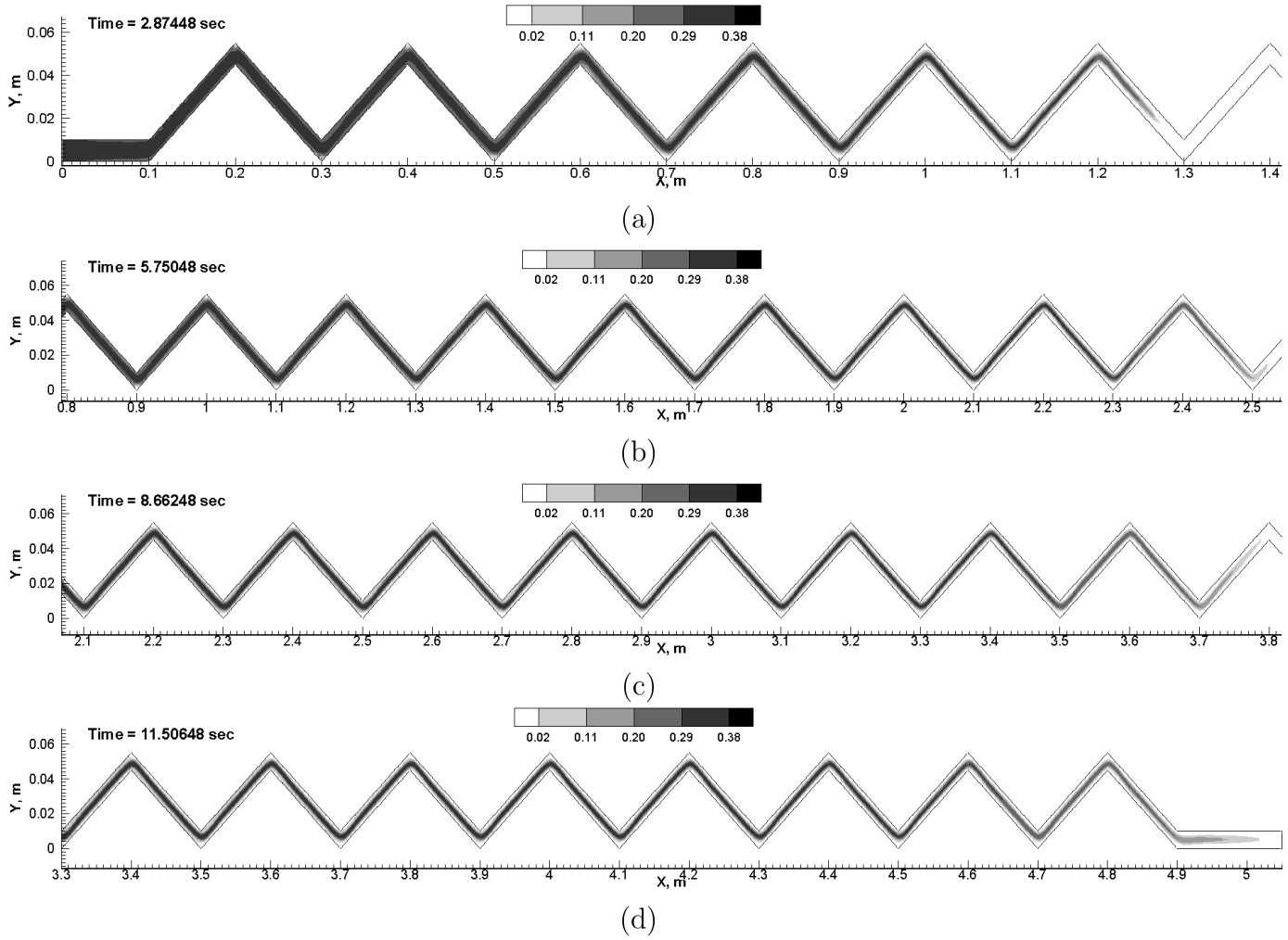

Figure 3.13: Contour plots of zikzak channel slurry flow 5 times viscous than regular with $e_{ss} = 0.90$ at different time t = a) 2.87 sec b) 5.75 sec c) 8.66 sec d)11.50 sec

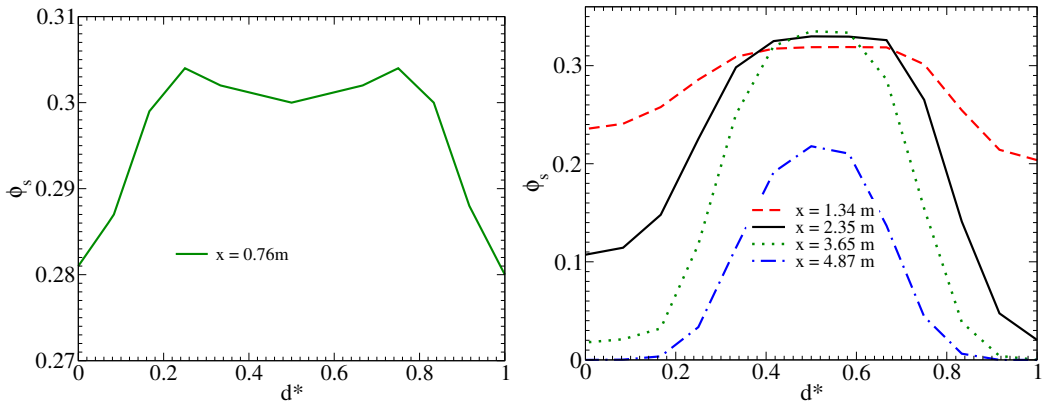

Figure 3.14: Volume fraction of particles for e_{ss}=0.90 in radial direction at a) t = 0.5 sec b) t= 11.50 sec in different axial location

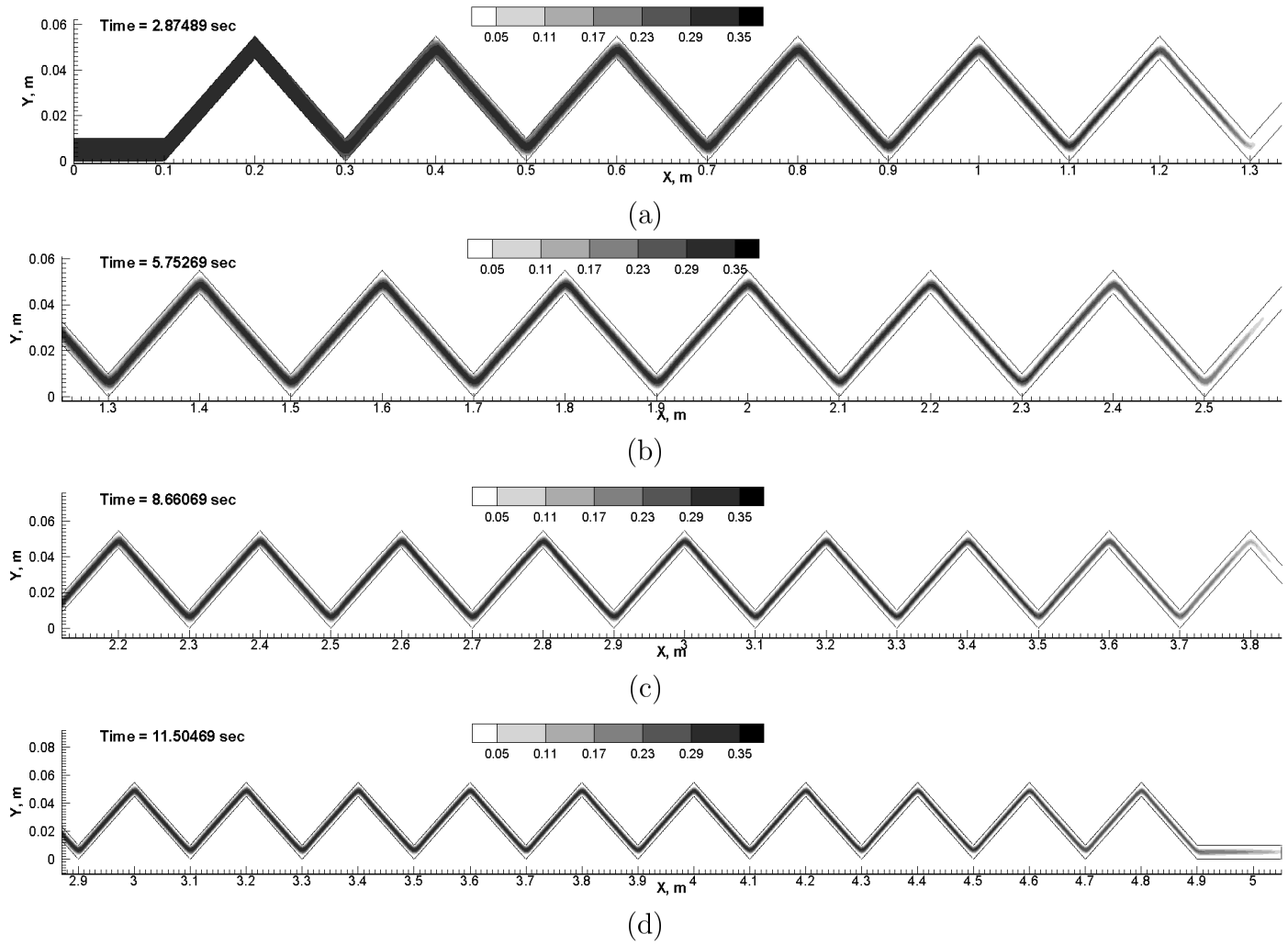

Figure 3.15: Contour plots of zikzak channel slurry flow 30 times viscous than regular with $e_{ss} = 0.90$ at different time t = a) 2.87 sec b) 5.75 sec c) 8.66 sec d)11.50 sec

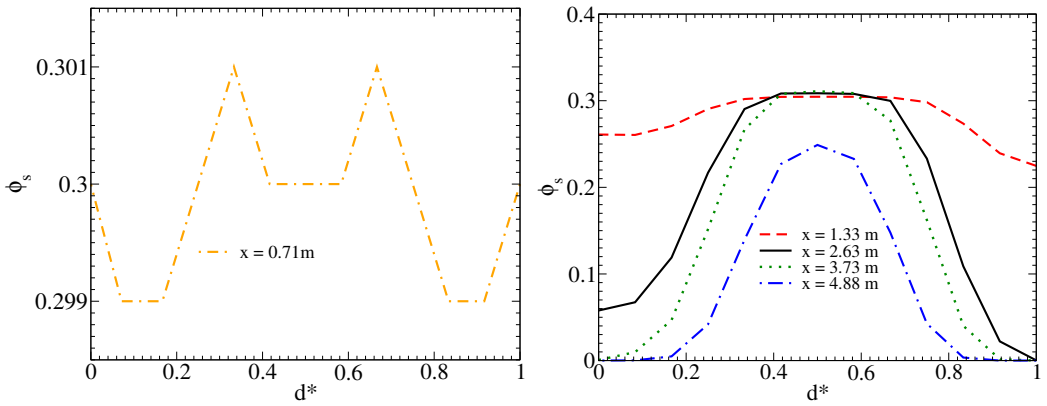

Figure 3.16: Volume fraction of particles for e_{ss}=0.90 at time a) t = 0.5 sec b) t= 11.50 sec in radial direction at different axial location

3.4.3 Mixing Zone

The mixing zone is a distance between the slurry front and a place where sand detaches the wall. We calculate mixing length, L_{mix} by measuring the distance visually from contour plot. To calculate L_{mix} for zikzak channel, we take the measurement of the path. That means we calculated the length of each angular portion and make sum of those to get the total mixing length. To better understand the propagation of mixing length L_{mix}, we plot mixing length against time for different case.

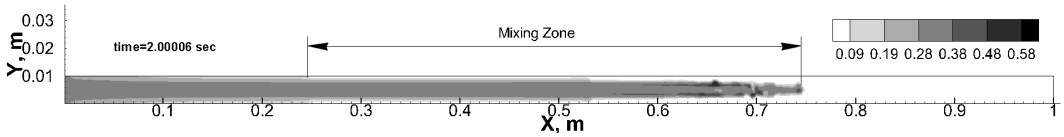

(a)

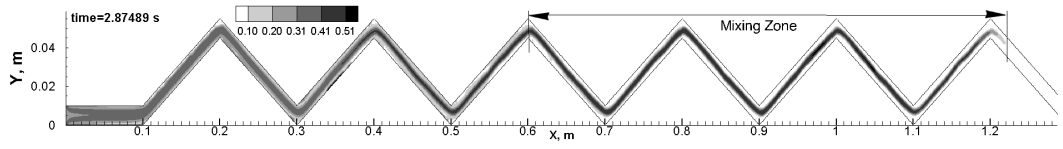

(b)

Figure 3.17: Indication of mixing zone for regularly viscous fluid in a) straight channel with e_{ss}=0.97 and b) zikzak channel with e_{ss}=0.90

Figure 3.17 indicates the mixing zone for a) straight and b) zikzak channel which was measured visually from the contour plot.

Figure 3.18 (a) shows the comparison of mixing length L_{mix} for zikzak and straight channel with e_{ss} =0.90 and viscous ratio of 1.0 while 3.18 (b) shows the comparison of mixing zone for zikzak channel with different viscous ratio. From 3.18 (a) we see that the mixing length is increasing with the increment

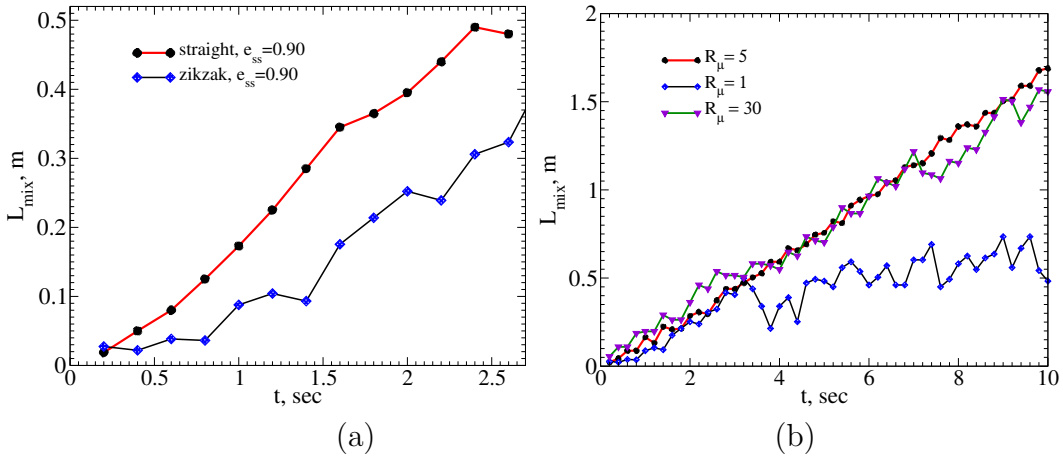

Figure 3.18: Change of mixing length with time for different case comparison a) comparison of fracture shape b) comparison of viscous ratio

of time and tends to follow a straight line up to 3 seconds for both straight and zikzak channel. For the straight channel, the slope of the line is higher than the slope of the zikzak channel. The reason behind this can be the propagation of mixing zone was restricted in the zikzak channel by the zikzak wall while such kind of restriction was absent for straight channel. We see from figure 3.18 (b) that the higher viscous ratio slurry almost follow a straight line with higher value of slope. But the viscous ratio of 1 shows very disturbed trend to follow straight line with much lower slope. Because we have seen previously that lower viscous ratio slurry moves with higher maximum volume fraction of particles reducing the propagation velocity of the flow. For this reason, the mixing length propagation for lower viscous ratio fluid is more disturbed and shows a lower slope of straight line. On the other hand, higher viscous ratio slurry moves fast because of lower maximum volume fraction of particles. When the viscous ratio is increased to 5, the slope is increased 200%. But when it is increase from 5 to 30, we don't see any significant change in slope.

3.4.4 Study of 3D Zikzak Shaped Fracture

Contour plot of 3D zizak shaped fracture .

Figure 3.19, 3.20 and 3.21 shows the contour plot of 3D zikzak channel for viscous ratio of 1, 5 and 30. We see here that the higher the viscous ratio, the lower the maximum volume fraction of particle. This scenario matches with our previous analysis done with 2d simulations. Most important information to be noticed here that we see the presence of instability of z-direction for lower viscous ration. With the higher viscous ratio, the instability decreases and for viscous ratio of 30, we see almost absence of instability in z direction. To better understand this phenomena, we plot volume fraction of particles in z-direction.

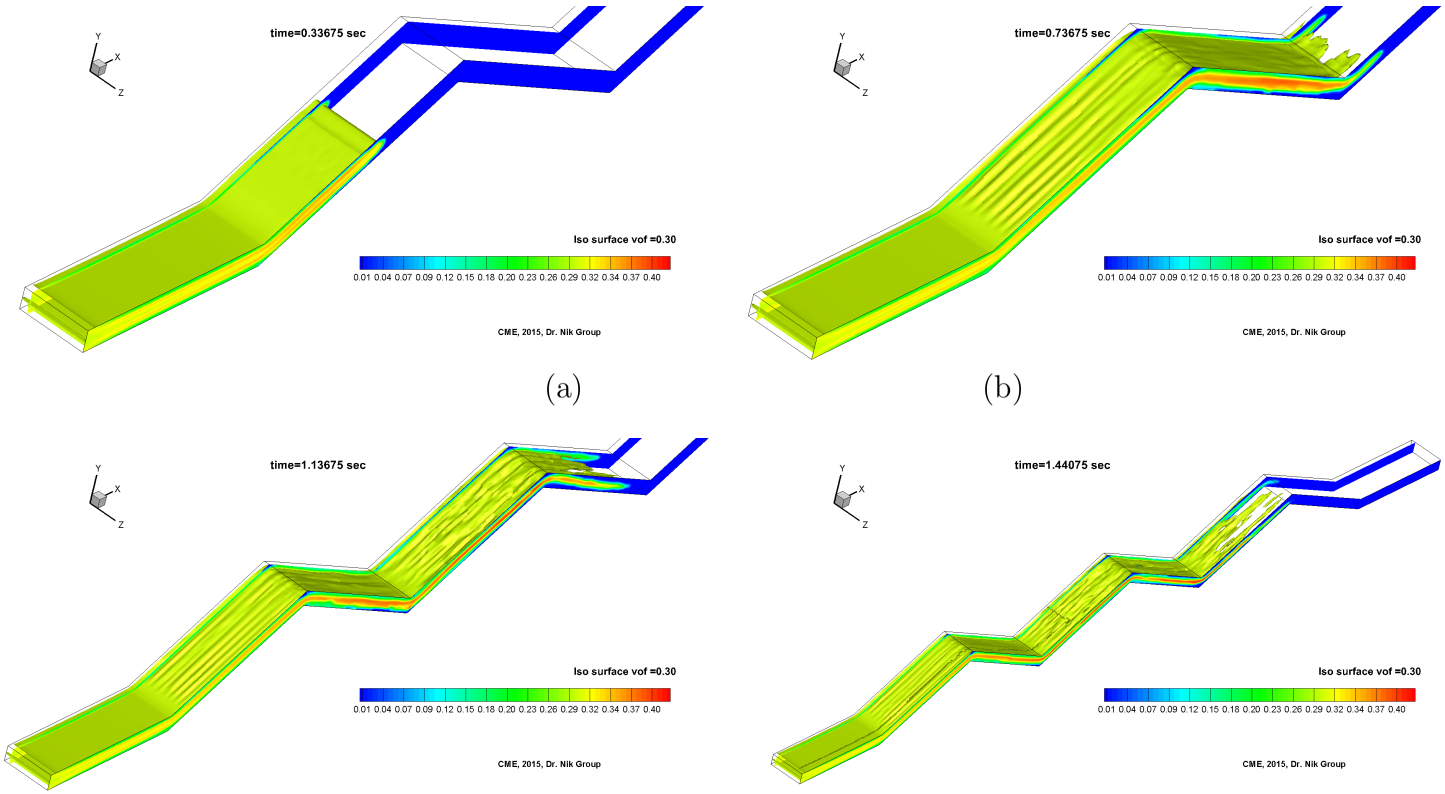

Figure 3.19: Contour plots of zikzak channel slurry flow regularly viscous fluid with $e_{ss} = 0.90$ for iso surface at volume of fraction =0.30 at different time t = a) 0.33 sec b) 0.73 sec c) 1.13 sec d)1.44 sec

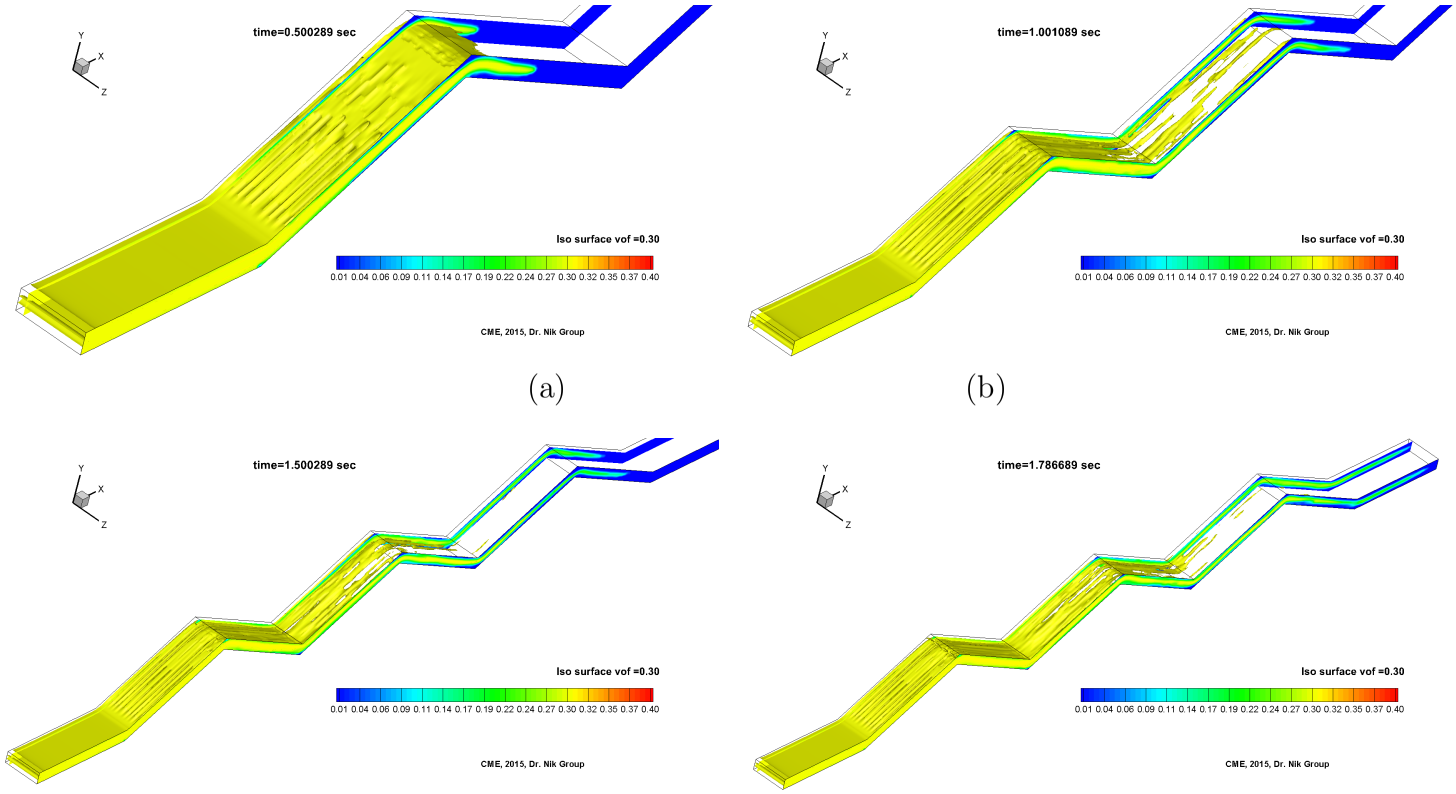

Figure 3.20: Contour plots of zikzak channel slurry flow with viscous ratio of 5 with $e_{ss} = 0.90$ for iso surface at volume of fraction =0.30 at different time t = a) 0.5 sec b) 1.0 sec c) 1.5 sec d)1.79 sec

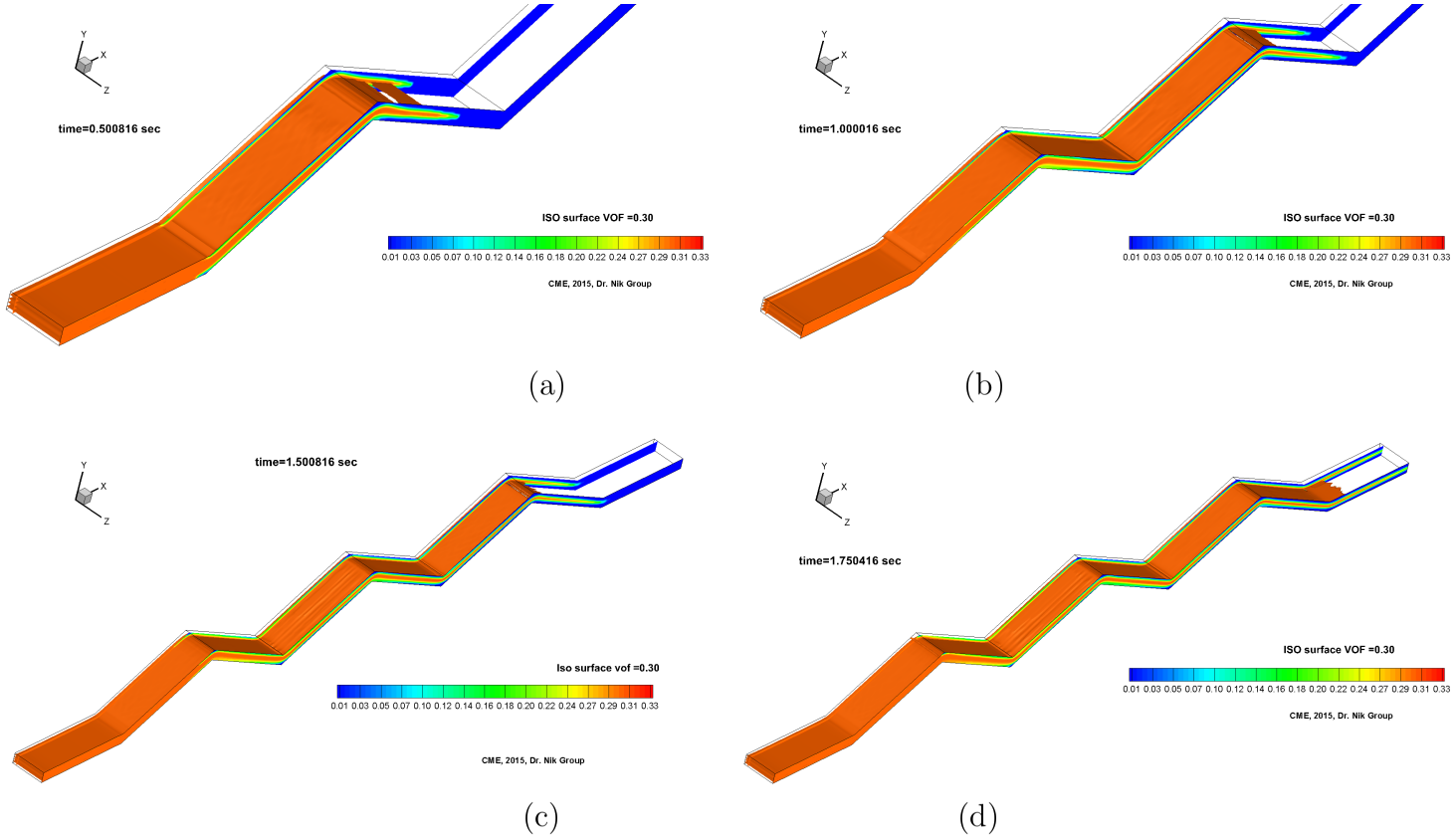

Figure 3.21: Contour plots of zikzak channel slurry flow with viscous ratio of 30 with $e_{ss} = 0.90$ for iso surface at volume of fraction =0.30 at different time t = a) 0.5 sec b) 1.0 sec c) 1.5 sec d)1.75 sec

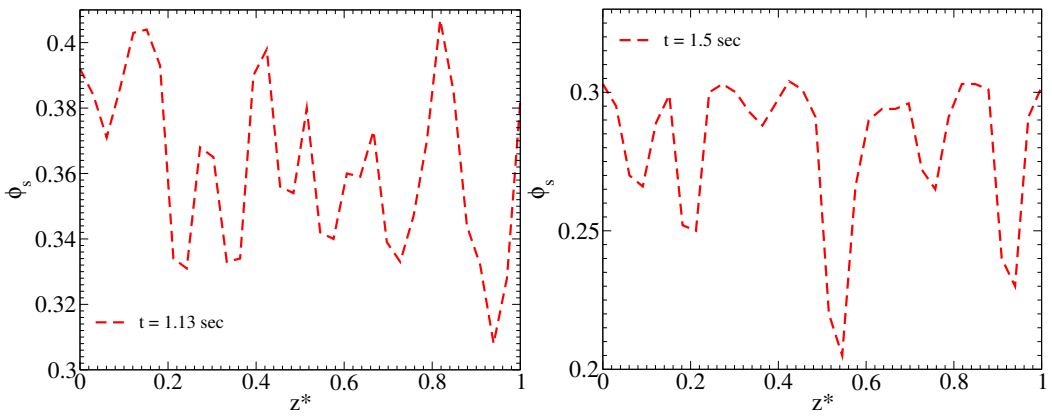

(a)

(b)

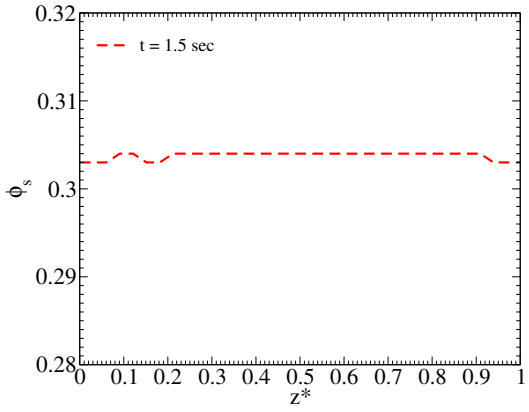

(c)

Figure 3.22: Volume fraction of particles regular viscous fluid for e_{ss}=0.90 (a) at time t= 11.50 sec in z-direction at x=0.45 m and y=0.0125 m (b) at time t= 11.50 sec in z-direction at x=0.45 m and y=0.0125 m (c) at time t= 11.50 sec in z-direction at x=0.45 m and y=0.0125 m

Figure 3.22 shows the volume fraction of particles in z-direction for viscous ratio of (a) 1 (b) 5 and (c) 30. We see here that for viscous ratio of 1 and 5, there is presence of instability. But the maximum amplitude of instability decreases with the increment of viscous ratio. On the other hand, for viscous

ratio of 30, the instability is minimum and can be rarely observed.

3.5 Summary

In this work we modeled CFD simulation of slurry transportation through a hydraulic fracturing. We used same Euler-Euler model that was utilized in chapter 2 for spout-bed modeling. We validated our model with Euler-Lagrange model for ice particle sedimentation. The results can be summarized as follows:

- The comparison of our Euler-Euler model with Euler-Lagrange model showed a very good agreement.
- From the plot of volume fraction of particles along the diameter we showed that the profile form an 'M' shape for both straight and zikzak shaped fracture. But this 'M' shape transformed into a parabolic profile for zikzak shaped fracture whereas, it remains unchanged for straight shaped fracture forming a higher pick with time.
- For straight shaped fracture, instability occurs sooner when restitution coefficient is increased.
- For zikzak shaped fracture, the maximum volume fraction decreases with the increment of viscous ratio.
- Mixing length almost linearly increases for both straight shaped fracture and for zikzak shaped fracture with higher viscous ratio. But with lower viscous ratio the slope of the line is lower with higher fluctuation.

- Finally we demonstrated 3d results for zikzak shaped fracture with different viscous ratio. We showed that for lower viscous ratio, the instability is present in z-direction. But with the increment of viscous ratio, the instability tends to become vanished.

3.6 Future Recommendation

The list of future recommendations for this study have been listed below:

- **Validation with experiment:** In our study, we validate our Euler-Euler model with Euler-Lagrange model for ice particle sedimentation. So, this model should be validated with experimental data to predict it's behaviour more accurately.

- **Different particle/liquid density:** Here, we have taken the same value of density for liquid and sand particles. Future work should be done by taking into account of the density of individual particle to represent real life flow more accurately.

- **Restitution coefficient:** Here we have taken restitution coefficient 0.90 for all of the cases. Future study should conduct to determine more accurate value of restitution coefficient for sand particles.

Chapter 4

Conclusions

This work attempts to develop Euler-Euler multiphase flow model for spouted bed and slurry transportation through hydraulic fracturing. In both cases we validated our model with available resources. Our findings states:-

- Comparisons were made between the experimental work done by He et. al. [1, 2], simulation using RANS turbulent model by Du et. al.[27, 5] and our simulation considering laminar flow.
  - Axial profiles of the time-averaged velocity of particles shows very good agreement with experimental results. Our simulation results slightly deviates from experiment at the beginning ($0 < z < 0.15m$), but matches exactly afterwards.
  - Comparison between Du et al [27, 5] work showed significant improvement of our model considering laminar flow with Syamlal-O'Brein [49] drag model. Our model predicted 15% improved result than Du et al [27, 5] RANS turbulent model.
  - Our model showed very good agreement for the radial profiles in

fountain zone. But we get acceptable results in spout zone. Simulations done by e_{ss} =0.90 and $\alpha_{s,max} = 0.61$ showed best agreement with experimental value.

  - Our model predicted spout profile successfully. Initially, simulation results matches with the experiment, but starts to deviate for higher bed height.

- Our main goal was to study the transient dynamics of spout bed.

  - We showed that the startup time is between 2-3 seconds.
  - The developed unsteady regime is reached after 4-5 seconds.

- We studied the influence of three different drag model on our simulation results. We compared axial profile time-averaged velocity of particles to do the comparison.

  - Gidaspow drag model [55] and Wen-Yu drag model [56] very similar result with slightly deviation. Gidaspow drag model showed around 3% improved result than Wen-Yu drag model [56].
  - Syamlal-O'Brein [49] dram model exhibited best result amongst these three models. With this model with restitution coefficient of e_{ss}, we get very good agreement with experiment. Syamlal-O'Brien [49] showed minimum of 30% improved result than the other two.

- We studied different basic model parameters such as coefficient of restitution e_{ss}, maximum packing limit $\alpha_{s,max}$, initial packing limit etc.

- We found that with the increment of restitution coefficient e_{ss} only by 5%, void space inside the system decreases to 18 %. Which decreases the maximum fountain height by 20% and maximum particle velocity along axial and radial direction by 40%.
- We also see that with slightly increment of maximum packing limit $\alpha_{s,max}$ and initial packing, the maximum velocity of particles along axial and radial direction increases. Though there was not any significant change of fountain height was observed.
- We also study the effect of e_{ss} on transient dynamics of spouted bed. We see here that with the increment of e_{ss}, the maximum amplitude of particles and gas decreases significantly. For lower value of e_{ss}, we get higher oscillation period.

- We analyzed the influence of swirling velocity to the spouted bed dynamics.
  - We found that for lower swirling ratio i. e. 0.136, we get better mixing of particles with slightly increased fountain height.
  - For higher swirling ratio i. e. 0.57, 1, we get lower fountain height. We also see the presence of Taylor-Goetler vortices for viscous ratio of 1.

- In another study, we modeled slurry transportation through a hydraulic fracturing.
  - We showed the presence of 'M' shaped profile along radial direction for volume fraction of particles in straight shaped fracture. We also see high particle concentration in the front of the slurry flow.

- For zikzak shaped fracture, similar 'M' shaped profile appeared at the beginning of the fracture, but disappeared afterwards.
- The length of mixing zone increases linearly with time. For straight shaped fracture, we get higher rate of increment whereas, for lower viscous ratio, we get lower rate of increment. For the increment of viscous ratio from 1 to 5, we get increment of slope around 50%.
- We also see the presence of instability on z-direction after analyzing the 3D zikzak shaped fracture. For higher viscous ratio, the instability reduces to an almost 'zero' value.

Bibliography

[1] Y.L. He, C.J. Lim, J. R. Grace, and J.X. Zhu. Measurements of voidage profiles in spouted beds. *The Canadian Journal of Chemical Engineering*, 72:229–234, 1994.

[2] Y. L. He, S. Z. Qin, C. J. Lim, and J. R. Grace. Particle velocity profiles and solid flow patterns in spouted beds. *The Canadian Journal of Chemical Engineering*, 72:561–568, 1994.

[3] ANSYS, Inc. ANSYS-FLUENT™ V 14.0 – Commercially available CFD software package based on the Finite Volume method. Southpointe, 275 Technology Drive, Canonsburg, PA 15317, U.S.A., www.ansys.com, 2013.

[4] F. Dierich, P.A. Nikrityuk, and S.Ananiev. 2d modeling of moving particles with phase-change effect. *Chem. Eng. Sci.*, 66:5459–5473, 2011.

[5] W. Du, X. Bao, J. Xu, and W. Wei. Computational fluid dynamics (cfd) modeling of spouted bed: Assessment of drag coefficient correlations. *Chemical Engineering Science*, 61:1401–1420, 2006.

[6] D. Eskin and M. Miller. A model of non-newtonian slurry flow in a fracture. *Powder Tech.*, 182:313–322, 2008.

[7] ANSYS Inc. *ANSYS-FLUENT® Theory Guide*, Release 14.0, 2013.

[8] Wikimedia Foundation, Inc. WIKIPEDIA ® – Free encyclopedia, "computer simulation", http://en.wikipedia.org/wiki/computer˙simulation, 2015.

[9] N. G. Deen, M. Van Sint Annaland, M. A. Van der Hoef, and J. A M Kuipers. Review of discrete particle modeling of fluidized beds. *Chemical Engineering Science*, 62:28–44, 2007.

[10] H. P. Zhu, Z. Y. Zhou, R. Y. Yang, and A. B. Yu. Discrete particle simulation of particulate systems: A review of major applications and findings, 2008.

[11] M.A. van der Hoef, M. van Sint Annaland, N.G. Deen, and J.A.M. Kuipers. Numerical Simulation of Dense Gas-Solid Fluidized Beds: A Multiscale Modeling Strategy, 2008.

[12] P. Doron, D. Granica, and D. Barnea. Slurry flow in horizontal pipesexperimental and modeling, 1987.

[13] G. B. Tupper, I. Govender, A. N. Mainza, and Neville Plint. A mechanistic model for slurry transport in tumbling mills. *Minerals Engineering*, 43-44:102–104, 2013.

[14] A Picot and C Lacroix. Production of multiphase water-insoluble microcapsules for cell microencapsulation using an emulsification/spray-drying technology. *Journal of Food Science*, 68:2693–2700, 2003.

[15] M. Mezhericher, A. Levy, and I. Borde. Probabilistic hard-sphere model of binary particle-particle interactions in multiphase flow of spray dryers. *International Journal of Multiphase Flow*, 43:22–38, 2012.

[16] Caixia Chen, Masayuki Horio, and Toshinori Kojima. Numerical simulation of entrained flow coal gasifiers. Part I: Modeling of coal gasification in an entrained flow gasifier. *Chemical Engineering Science*, 55:3861–3874, 2000.

[17] A. Chinnayya, A. Chtab, J. Q. Shao, R. M. Carter, Y. Yan, and S. Caillat. Characterization of pneumatic transportation of pulverised coal in a horizontal pipeline through measurement and computational modelling. *Fuel*, 88:2348–2356, 2009.

[18] Yanxiang Chen, Guilan Wang, and Haiou Zhang. Numerical simulation of coating growth and pore formation in rapid plasma spray tooling. *Thin Solid Films*, 390:13–19, 2001.

[19] P S Grant. Spray forming. *Progress in Materials Science*, 39:497–545, 1995.

[20] Jian Hao, Tsorng Whay Pan, Roland Glowinski, and Daniel D. Joseph. A fictitious domain/distributed Lagrange multiplier method for the particulate flow of Oldroyd-B fluids: A positive definiteness preserving approach. *Journal of Non-Newtonian Fluid Mechanics*, 156:95–111, 2009.

[21] T.-W. Pan, D. D. Joseph, R. Bai, R. Glowinski, and V. Sarin. Fluidization of 1204 spheres: simulation and experiment, 2002.

[22] T. W. Pan, D. D. Joseph, and R. Glowinski. Modelling RayleighTaylor instability of a sedimenting suspension of several thousand circular particles in a direct numerical simulation, 2001.

[23] Bodhisattwa Chaudhuri, Fernando J. Muzzio, and M. Silvina Tomassone. Modeling of heat transfer in granular flow in rotating vessels. *Chemical Engineering Science*, 61:6348–6360, 2006.

[24] Deliang Shi, Watson L. Vargas, and J. J. McCarthy. Heat transfer in rotary kilns with interstitial gases. *Chemical Engineering Science*, 63:4506–4516, 2008.

[25] Jesse Capecelatro and Olivier Desjardins. An Euler-Lagrange strategy for simulating particle-laden flows. *Journal of Computational Physics*, 238:1–31, 2013.

[26] P. Sreekanth, M. Syamlal, and T.J. O'Brien. *Computational Gas-Solid Flows and Reacting Systems: Theory, Methods and Practice*. IGI Global, 2011.

[27] W. Du, X. Bao, J. Xu, and W. Wei. Computational fluid dynamics (cfd) modeling of spouted bed: Influence of frictional stress, maximum packing limit and coefficient of restitution of particles. *Chemical Engineering Science*, 61:4558–4570, 2006.

[28] W. Zhonghua and A.S. Mujumdar. CFD modeling of the gas-particle flow behavior in spouted beds. *Powder Technology*, 183:260–272, 2008.

[29] R. Bettega, R. Guimaraes, and J.T. Freire. Scale-up study of spouted beds using computational fluid dynamics. *2009*, 87:193–203, 2009.

[30] K.G. Santos, V.V. Murata, and M.A.S. Barrozo. Three-dimensional computational fluid dynamics modelling of spouted bed. *Can. J. Chem. Eng.*, 87:211–219, 2009.

[31] R. Bettega, A.R.F. de Almeida, R. G. Correa, and J. T. Freire. CFD modelling of a semi-cylindrical spouted bed: numerical simulation and experimental verification. *Can. J. Chem. Eng.*, 87:177–184, 2009.

[32] X. Liu, W. Zhong, Y. Shao, B. Ren, and B. Jin. Evaluation on the effect of conical geometry on flow behaviours in spouted beds. *2014*, 92:768–774, 2014.

[33] K.B. Mathur and P.E. Gishler. A technique for contacting gases with coarse solid particles. *AIChE*, 1:157–164, 1955.

[34] M. Goldschmidt, J. Kuipers, and W. Swaaij. Hydrodynamic modeling of dense gas-fluidised beds using the kinetic theory of granular flow: effect of coefficient of restitution on bed dynamics. *Chemical Engineering Science*, 56:571–578, 2001.

[35] Lu Huilin, He Yurong, Liu Wentie, Jianmin Ding, Dimitri Gidspow, and Jacques Bouillard. Computer simulations of gas-solid flow in spouted beds using kinetic-frictional stress model of granular flow. *Chemical Engineering Science*, 59:865–878, 2004.

[36] L. Qian, Y. Lu, W. Zhong, X. Chenand B. Ren, and B. Jin. Developing a novel fibre high speed photography method for investigating solid volume fraction in a 3d spouted bed. *Can. J. Chem. Eng.*, 91:1793–1799, 2013.

[37] H. Xu, W. Zhong, B. Jin, and J. Wang. Flow pattern and transition in gas-liquidsolid three phase spouted bed. *Int. J. Powd. Tec.*, 267:18–25, 2014.

[38] J.M. Link, L.A. Cuypers, N.G. Deen, and J.A.M. Kuipers. Flow regimes in a spout-fluid bed: A combined experimental and simulation study. *Chem. Eng. Sci.*, 60:3425–3442, 2005.

[39] J. M. Link, C. Zeilstra, N.G. Deen, and J.A.M. Kuipers. Validation of a discrete particle model in a 2d spout-fluid bed using non-intrusive optical measuring techniques. *The Can. Jour. of Chem. Eng.*, 82, 2004.

[40] R. Bettega, A.R.F. de Almeida, R. G. Correa, and J. T. Freire. CFD modelling of a semi-cylindrical spouted bed: numerical simulation and experimental verification. *Can. J. Chem. Eng.*, 87:177–184, 2009.

[41] R. Bettega, R. Guimaraes, and J.T. Freire. Scale-up study of spouted beds using computational fluid dynamics. *2009*, 87:193–203, 2009.

[42] Y.-L. He, C.J. Lim, and J.R. Grace. Scale-up studies of spouted beds. *Chem. Eng. Sci.*, 52:329–339, 1997.

[43] O. Gryczka, S. Heinrich, N. G. Deen, M. V. S. Annaland, J. A. M. Kuipers, and L. Morl. Cfd modeling of a prismatic spouted bed with two adjustable gas inlets. *Can. J. Chem. Eng.*, 87:318–328, 2009.

[44] R. Clift, J. R. Grace, and M. E. Weber. *Bubbles, Drops and Particles*. Academic Press, NewYork, 1978.

[45] G. Hradil P. A. Shirvanian, J. M. Calo. Numerical simulation of fluid-particle hydrodynamics in a rectangular spouted vessel. *Int. J. of Multiphase Flow*, 32:739–753, 2006.

[46] W. Zhonghua and A. S. Mujumdar. Cfd modeling of the gas- particle flow behavior in spouted beds. *Int. J. of Powder Tech.*, 183:260–272, 2008.

[47] Norman Epstein and John R Grace. *Spouted and spout-fluid beds: fundamentals and applications*. Cambridge University Press, 2010.

[48] M. Syamlal. The particle-particle drag term in a multiparticle model of fluidization. Technical Report DOE/MC/21353-2373, NTIS/DE870065001987, National Technical Information Service.

[49] M Syamlal and TJ Obrien. Computer simulation of bubbles in a fluidized bed. In *AIChE Symposium Series*, volume 85, pages 22–31, 1989.

[50] C.K.K. Lun, S.B. Savage, D.J. Jeffrey, and N. Chepurniy. Kinetic theories for granular flow: Inelastic particles in couette flow and slightly inelastic particles in a general flow field. *J. Fluid Mech.*, 140:223–256, 1984.

[51] P. C. Johnson and R. Jackson. Frictional-collisional constitutive relations for granular materials, with application to plane shearing. *J. Fluid Mech.*, 176:67–93, 1987.

[52] Satoru Ogawa, Akira Umemura, and Nobunori Oshima. On the equations of fully fluidized granular materials. *Zeitschrift f??r angewandte Mathematik und Physik ZAMP*, 31:483–493, 1980.

[53] S. Muzaferija, M. Peric, P. Sames, and T. Schellin. A two-fluid navier-stokes solver to simulate water entry. In *In Proc 22nd Symposium on Naval Hydrodynamics*, 277-289, 1998.

[54] B.P. Leonard. A stable and accurate convective modeling procedure based on quadratic upstream interpolation. *Compu. Methods Appl. Mech. Eng.*, 19:59–98, 1979.

[55] Dimitri Gidaspow. *Multiphase flow and fluidization: continuum and kinetic theory descriptions*. Academic press, 2012.

[56] C. Y. Wen and Y. H. Yu. Mechanics of fluidization. *Chemical Engineering Progress, Symposium Series*, 62:100–111, 1966.

[57] Mo Syamlal. The particle-particle drag term in a multiparticle model of fluidization. *National Technical Information Service, Springfield, VA*, 188, 1987.

[58] M.J. Economides and K.J. Nolte. *Reservoir Stimulation*. Schlumberger, 2000.

[59] J G Swadener and N C Huang. An investigation of hydraulic fracturing .2. 2-phase flow model. *Theoretical and Applied Fracture Mechanics*, 18:103–113, 1993.

[60] Alexander M. Linkov. On efficient simulation of hydraulic fracturing in terms of particle velocity. *International Journal of Engineering Science*, 52:77–88, 2012.

[61] A. A. Savitski and E. Detournay. Propagation of a penny-shaped fluid-driven fracture in an impermeable rock: Asymptotic solutions. *International Journal of Solids and Structures*, 39:6311–6337, 2002.

[62] S Ouyang, G F Carey, and C H Yew. An adaptive finite element scheme for hydraulic fracturing with proppant transport. *International Journal for Numerical Methods in Fluids*, 24:645–670, 1997.

[63] Finite Element Solution, A Boundary, Integral Equation, F O R Mode, Embedded Three, and Dimensional Fractures. Integral equation for mode I embedded three. 26(July 1987):1525–1540, 1988.

[64] J. I. Adachi and E. Detournay. Self-similar solution of a plane-strain fracture driven by a power-law fluid. *International Journal for Numerical and Analytical Methods in Geomechanics*, 26:579–604, 2002.

[65] J. Adachi, E. Siebrits, A. Peirce, and J. Desroches. Computer simulation of hydraulic fractures. *International Journal of Rock Mechanics and Mining Sciences*, 44:739–757, 2007.

Appendix

A short list of important experimental and simulation works are presented in tabular form below:

Name	*Contribution*
He at. el. [1]	Authors experimentally measured the profiles of vertical particle velocities in the spout and the fountain of a half-column and full-column spouted bed. To determine the spout-annulus interface and to measure vertical particle velocities in the annulus of the full-columns authors used a fiber optic image probe in the annulus of the full-column. They found that, radial profiles of vertical particle velocities were of near Gaussian distribution. Under identical operating conditions, particle velocities along the spout axis in the half-column were 30% lower than in the full-column. The fountain core expanded suddenly near the bed surface and then gradually contracted with height.
He at. el. [2]	In another work He at. el. and co-authors measured voidage profiles in the fountain, spout and annulus of spouted beds. They found that the voidage in the annulus is higher than the loose-packed voidage and that it increase with increasing gas flow rate; except for a restricted region near the spout-annulus interface. They also found that the voidage is lower than the loose-packed bed voidage in the denser region of the annulus near the spout interface. Local voidage decreases with height and radial distance from the spout axis in spout region.

Table 1: List of the summary of important experimental contribution on spouted bed

Name	*Model*	*Software*	*Contribution*
Du at. el. [27, 5]	E-E	Fluent	Du and co-workers carried out numerous CFD-based simulations of spouted bed in respect to the influence of different drag models, maximum packing limit, coefficient of restitution on the characteristics of the spouted bed investigated experimentally by He et. al. [1, 2]. Authors used RANS-based Euler-Euler model. The comparison against experimental data by He et al. showed qualitative agreement. They found that the frictional stress is important in the annulus and has a slight effect on the hydrodynamics of the flow in the spout region. The maximum packing limit affects the radial distribution function and thereby impacts the estimation of the properties of the pseudo-fluid phase of the particles. They also found that the strong dependence of the granular temperature on the coefficient of restitution accounts for the influence of the latter on the CFD modeling of the spouted bed.
Link at. el. [38]	E-L	DPM code	Authors took an attempt to design a model which has the ability to reproduce several important regimes in spout-fluid bed. The model was capable of predicting appropriate regimes in most of the cases. Their model could predict the frequency at which the largest power was found. But the limitation of the model was, it could not predict any large slugs in the slugging bed regime.

Table 2: List of the summary of important contribution in CFD modeling of spouted bed